Department of Physics and Astronomy
University of Heidelberg

Bachelor Thesis in Physics
submitted by

Nicolas Schmidt

born in Starnberg (Germany)

2014

Neutral Pion Measurements with Conversions in ALICE in pp Collisions at $\sqrt{s} = 8$ TeV

This Bachelor Thesis has been carried out by Nicolas Schmidt at the
Physikalisches Institut at the University of Heidelberg
under the supervision of
PD Dr. Klaus Reygers

Abstract

In this thesis the differential invariant cross section and the differential invariant yield of π^0 mesons for proton-proton collisions at $\sqrt{s} = 8$ TeV from the data taking campaign in 2012 is presented. The mesons are measured by reconstructing their decay photons from electron-positron pairs with the information of the Inner Tracking System and the Time Projection Chamber. The statistics provided by the dataset allows a π^0 signal extraction over a range of $0.4 < p_{\mathrm{T}} < 8$ GeV/c and the resulting spectra are corrected using PHOJET and PYTHIA8 Monte Carlo Simulations. For the dataset a systematic error estimation is performed which leads to a total systematic error of 9.5-11%. In addition the spectra are compared to results from lower center of mass energy measurements at $\sqrt{s} = 7$, 2.76 and 0.9 TeV. This comparison includes the evolution of the parameters of the Tsallis function and Powerlaw fitted to the corrected spectra. A clear flattening of the spectra at high p_{T} is seen with increasing energy, while the total yield increases at the same time. Finally the influences of the TRD and EMCal triggers on the photon and π^0 meson raw yield are studied.

Zusammenfassung

In dieser Arbeit wird der invariante Wirkungsquerschnitt und das Transversalimpulsspektrum von π^0 Mesonen in Proton-Proton Kollisionen bei einer Schwerpunktsenergie von $\sqrt{s} = 8$ TeV aus Messungen von 2012 präsentiert. Die Mesonen werden gemessen, indem ihre Zerfallsphotonen aus Elektron-Positron Paaren, mithilfe der Informationen aus dem Inner Tracking System und der Time Projection Chamber, rekonstuiert werden. Die Statistik des verwendeten Datensets ermöglicht eine Extraktion des π^0 Signals über eine Spanne von $0.5 < p_{\mathrm{T}} < 8$ GeV/c und die resultierenden Spektren werden mit Hilfe von PHOJET und PYTHIA8 Monte Carlo Simulationen korrigiert. Für das Datenset wird zudem eine Abschätzung der systematischen Fehler durchgeführt, welche zu einem systematischen Gesamtfehler von 9.5-11% führt. Zusätzlich werden die Spektren mit den Ergebnissen von Messungen niedrigerer Schwerpunktsenergien mit $\sqrt{s} = 7$, 2.76 and 0.9 TeV verglichen. Dieser Vergleich behinhaltet die Entwicklung der Parameter der Tsallis Funktion und des Potenzgesetzes, welche an die korrigierten Spektren angeglichen wurden. Mit steigender Energie ist eine deutliche Abflachung der Spektren zu hohem p_{T} zu sehen, wobei die gesamte Produktion sich zugleich erhöht. Zuletzt wird der Einfluss der TRD und EMCal Trigger auf die Photonen und π^0 Transversalimpulsspektren untersucht.

Contents

1 Introduction

The Large Hadron Collider (LHC) allows for new dimensions in high energy proton-proton (pp) and heavy ion collisions (A-A). Reaching up to a maximum design value of 14 TeV center of mass energy in pp [30], it is more powerful than every other accelerator before and even outruns the Tevatron which reached a center of mass energy of 2 TeV.

The LHC energies allow for Standard Model studies, probing of new theories and the creation of a new state of matter, the Quark-Gluon Plasma (QGP). The QGP could provide information about how the early universe was 10 ps to 10 μs after the Big Bang [35]. Furthermore it allows studies of the Quantum Chromodynamics (QCD) which describes the strong interaction of matter, but as the QGP only lasts for a short duration and is relatively small, every measurement of it can only be done by using particles that are created in the collision itself. The π^0 meson and its suppression is one of these probes for the QGP and therefore plays an important role in extracting information from this medium.

In this thesis the production of neutral pions in proton-proton collisions at $\sqrt{s} = 8$ TeV will be described. The measurement from this collision energy provides a test of the applicability of perturbative QCD (pQCD) at this energy. The measured π^0 spectrum is also essential to the direct-photon measurement from the strong decay background which comes mainly from the π^0 and η decay. Furthermore it will be used for an interpolation of a 5 TeV reference for the 2015 Pb-Pb runs. There the new data could be used as a second high energy reference besides 7 TeV and therefore improve the determination of the energy dependence of the interpolation.

1.1 The Standard Model

The Standard Model is the theory describing the fundamental particles and how they interact through the electromagnetic, strong and weak interaction force [19].

Figure 1 shows an overview of the fundamental particles including the Higgs boson which is needed as an exchange particle of the higgs mechanism. The fundamental particles are split into two categories, the fermions with half-integer spin and the bosons with integer spin. Fermions are further divided into leptons and quarks. For each of these particles, an anti-particle with the same mass but with opposite charge exists. On the other hand, the quarks experience strong interaction and carry a charge of +2/3 or -1/3 instead of ±1. The leptons can further be splitted into two categories, the massless and chargeless neutrinos $\nu_{e,\mu,\tau}$ and the leptons which carry mass and charge (e, μ, τ) [19, 44].
The gauge bosons (γ, g, W, Z) are the particles carrying the fundamental forces. While gluons are transfer the strong interaction, photons do the same for the electromagnetic force and the $W^{\pm}$ and Z^0 bosons for the weak interaction.

1.2 Quantum Chromodynamics

The theory of the strong interaction is QCD [33, 47] which only involves quarks and gluons. A quark itself can exist in three different colors which together form a color

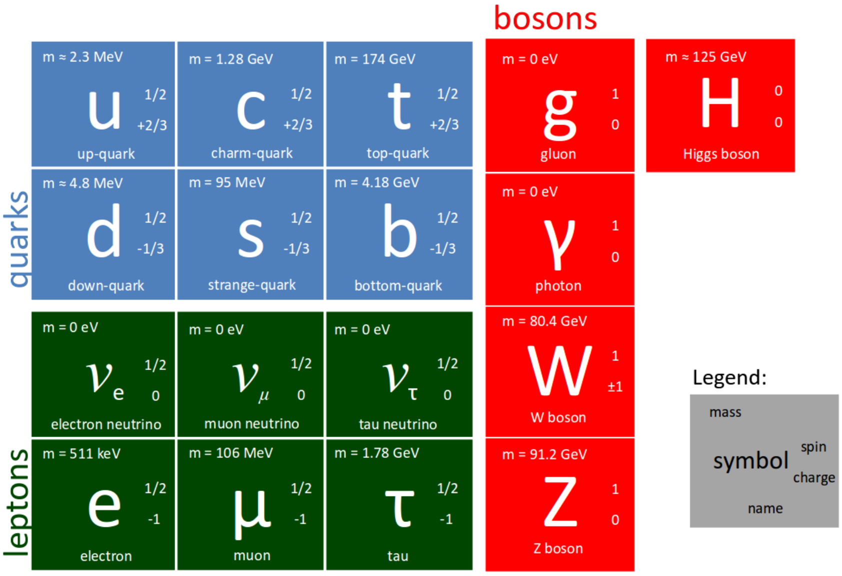

Figure 1: Fundamental particles of the Standard Model.[44]

triplet. This color in the strong interaction can be considered like the charge in the electromagnetic interaction. In addition there are also anti-quarks with anti-colors, but independent from the color, the strength of the color charge itself is the same for all three colors. It is important that a bound state of quarks and gluons will be colorless for an observer. These colorless particles can be split into baryons with three quarks, where each quark carries a different color and mesons which consist of one quark and one antiquark. The Lagrange density of QCD [34, 47] is given by

$$\mathcal{L} = \sum_q \overline{\psi_q} \gamma^\mu \left(i\partial^\mu - g_s A_a^\mu \frac{\lambda_a}{2} \right) \psi_q - \sum_q m_q \overline{\psi_q} \psi_q - \frac{1}{4} \sum_a F_a^{\mu\nu} F_{\mu\nu,a} \tag{1}$$

where ψ_q corresponds to the quark field, g_s to the effective strong charge, A_q^μ to a gluon field, λ_a to the Gell-Mann matrices [27] and the gluon field strength tensor which is given by $F_a^{\mu\nu} = \partial^\mu A_a^\nu - \partial^\nu A_a^\mu + i g_s f_{abc} A_\mu^b A_\nu^c$.

The invariance of the QCD Lagrangian for massless particles under the exchange of left- and right-handed components of the quark spinor is called *chiral symmetry*. With quarks being particles with mass, this symmetry is explicitly broken. Even for massless quarks, the strong force between quarks and anti-quarks leads to a rise of a so-called *chiral condensate*, which is not invariant under the exchange of left- and right-handed fermions. The chiral symmetry of the QCD Lagrangian is therefore spontaneously broken, which leads to massless bosons with spin 0 that are called *Goldstone bosons*. These can be identified with the lightest mesons (π^0, $\pi^\pm$, $K^\pm$, K^0, $\overline{K^0}$, η, η') [18].

The coupling strength of quarks g_s in QCD can be written as $\alpha_s = g_s^2/4\pi$ [34] while α_s has to be determined from experiments as QCD is unable to predict its value. Depending on the momentum transfer (Q) α_s is larger than the Quantum Electrodynamics (QED) coupling constant ($\alpha_{\text{em}} \approx \frac{1}{137}$). The Q dependence of α_s in the leading order can be expressed as

$$\alpha_s(Q^2) \approx \frac{12\pi}{(33 - 2N_f)\ln\frac{Q^2}{\Lambda^2}} \tag{2}$$

with N_f being the number of quark flavors and Λ being the QCD scaling parameter. Experiments determined Λ to be about 200 MeV. The equation above can only be used if $Q^2 \gg \Lambda^2$.

Between a pair of quarks ($q\overline{q}$) there is a phenomenological potential which can be approximated as

$$V_s = -\frac{4}{3}\frac{\alpha_s}{r} + kr. \tag{3}$$

where the distance between the quarks is expressed by r. This leads to two important consequences, on the one hand for small r the first term is dominant and behaves like a Coulomb-interaction, on the other hand with increasing r the potential grows linearly which leads to the fact that one would need an infinite amount of energy to remove a quark completely from a bound state. This is the reason why at a certain point a new quark-anti-quark pair will be created from the vacuum which is called *confinement*. Another consequence is the so called *asymptotic freedom* which happens at high energies and short distances with high momentum transfers ($Q \to \infty$), there the coupling strength decreases and the particles can behave like free particles.

The theory of Quantum Chromodynamics (QCD) considers hadronic matter to be made out of quarks which interact with each other by exchanging gluons. Those quarks and gluons carry a color charge which is conserved in all processes and both particles will always form colorless mesons and baryons. So far no color charged particle has been observed and therefore leads to a confinement property in QCD which does not allow free colored objects.[36]

1.3 The Quark Gluon Plasma

The high temperatures and energy densities in the QGP weaken the confinement condition by an extend that allows quarks and gluons to be deconfined and therefore not bound in hadrons. Even though the particles in the medium can exist with an unbalanced color charge, the medium itself must be neutral in color.
The production of this medium is driven by a large amount of energy in a small amount of space which is expected to have been the case shortly after the Big Bang. To study what happened there, we need to focus on the experimental creation of such a medium.[26]
Ideally, this creation is archived in heavy ion collisions at high energies where the critical temperature T_c is reached which has been estimated to be about 100-250 MeV [40]. Experiments reaching this temperature have been performed for example at the Super Proton Synchrotron (SPS), the Relativistic Heavy Ion Collider (RHIC) and the LHC. Figure 2 shows the freeze-out temperatures of the QGP the different experiments could reach. It can also be seen that at low T and μ_B nuclear matter shows confinement and hadrons are the degrees of freedom. At higher T a phase transition to a deconfined quark gluon plasma with restored chiral symmetry is predicted by Lattice QCD (LQCD). The phase transition might exhibit a critical point at about $\mu_B \sim 700$ MeV. More exotic

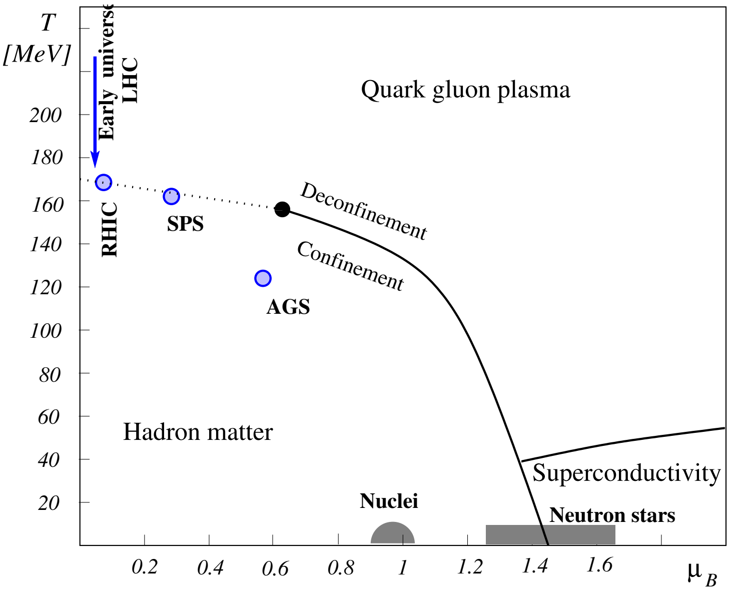

Figure 2: Schematic QCD phase diagram in the $T - \mu_B$ plane. [32]

quark phases can occur at high density, e.g. in the interior of very dense neutron stars. Chemical freeze-out conditions reached in heavy ion experiments at Alternating Gradient Synchrotron (AGS), SPS and RHIC are also indicated. The blue arrow along the T axis shows how the matter is supposed to evolve at LHC before freeze-out, starting at very high temperature. The evolution of the early universe a few microseconds after the big bang took a similar path.

Due to the extended profile of heavy nuclei, many nucleons collide during one collision and therefore produce many interacting particles. The fireball of this collision and and its high temperature allow for deconfinement of the quarks. The fireball starts to expand after its creation. As soon as it has expanded until the temperature drops below the critical temperature, the matter again recombines into color-neutral particles. This process is called hadronization.

One possibility to explain high multiplicity pp events that show collective behavior is a small QGP which is produced. But there are also other possibilities like mini-jets [21] or ridges [51] which could explain the same behavior with a different kind of physics. Due to the interaction of only two nucleons in proton-proton collisions compared to more than 300 in central lead-lead collisions a QGP in pp collisions would be much smaller. For a short thermalization time, e.g. $\tau_0 < 0.5$ fm, a mini-QGP with sizes of $\sim$2-3 fm could be formed.[55]

1.4 The Neutral Pion π^0

The π^0 is the lightest meson as it is a superposition of the two quantum states $|\pi^0\rangle = \frac{1}{\sqrt{2}}\left(|u\bar{u}\rangle - |d\bar{d}\rangle\right)$ and has a mass of about 134.976 MeV/c^2. Being the lightest meson, the π^0 cannot decay into other mesons. Its lifetime is $(8.52 \pm 0.18) \cdot 10^{-17}$ s and it decays electromagnetically to $\pi^0 \to \gamma\gamma$ with a branching ratio (BR) of 98.823% or via the Dalitz-decay channel to $\pi^0 \to \gamma + e^+e^-$ with BR 1.174%.

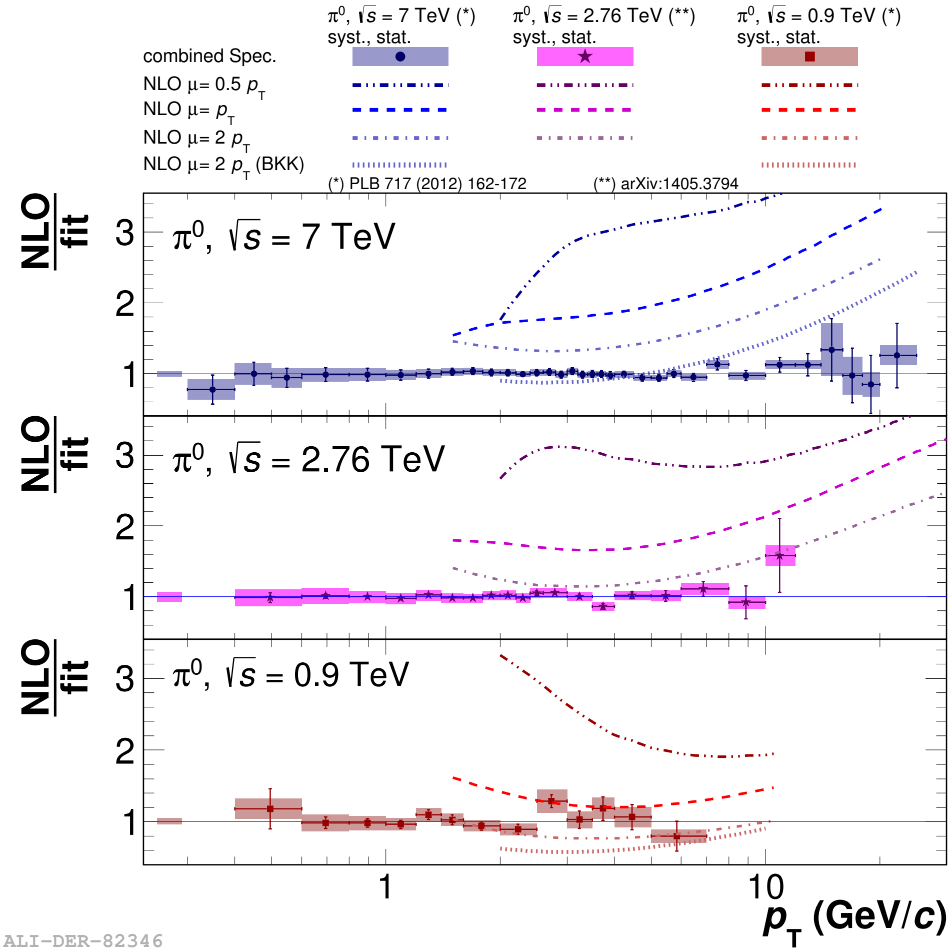

ALI-DER-82346

Figure 3: Ratio of the NLO calculations to the π^0 meson data spectrum in 0.9, 2.76 & 7 TeV pp collisions.[3]

Due to its clear peak in the gamma-gamma channel the π^0 is easy to identify and even with weak photon identification cuts it can still be extracted and analyzed.

In order to investigate the QGP a well known particle is required. One possibility is the use of the neutral pion π^0 and its suppression due to the presence of the medium. As the medium is very extended and dense in heavy ion collisions it can decrease the particle production by up to 90%. The proton-proton collisions with a small and more or less negligible QGP on the other hand can be used as a reference for further calculations and comparisons. One important factor in this case is the jet quenching where the jets that are produced by high energy particles interact with the medium and loose a significant amount of energy. It can be described with the nuclear modification factor R_{AA}. This factor is defined as the ratio of the production cross sections in heavy ion collisions and pp collisions scaled by the number of binary collisions N_{coll}.

$$R_{AA}(p_{\mathrm{T}}) = \frac{(1/N_{\mathrm{AA}}^{\mathrm{evt}})\mathrm{d}^2 N_{\mathrm{AA}}^{\pi^0}/\mathrm{d}p_{\mathrm{T}}\mathrm{d}y}{\langle T_{\mathrm{AB}}\rangle \times \mathrm{d}^2\sigma_{\mathrm{pp}}^{\pi^0}/\mathrm{d}p_{\mathrm{T}}\mathrm{d}y} \tag{4}$$

The scaling factor for the pp π^0 cross section is called the nuclear overlap function $\langle T_{\mathrm{AB}}\rangle$ which is defined as the average number of binary collisions divided by the inelastic pp cross section.

$$\langle T_{\mathrm{AB}}\rangle = \langle N_{\mathrm{coll}}\rangle / \sigma_{\mathrm{pp}}^{\mathrm{inel}} \tag{5}$$

If R_{AA} shows a decrease from unity, this is interpreted as a loss of parton momentum due to the processes that take place in heavy ion collisions, e.g. gluon bremsstrahlung [15]. Therefore to get good results when analyzing heavy ion collisions a precise reference particle yield from pp collisions is very important. In this thesis the π^0 meson yield at $\sqrt{s} = 8$ TeV is extracted and could be used as an additional reference point for the interpolation with the already existing results from $\sqrt{s} = 900$ GeV, $\sqrt{s} = 2.76$ TeV and $\sqrt{s} = 7$ TeV to get a good reference for the 2015 Pb-Pb runs.

In Figure 3 it can be seen that the Next-to-Leading Order (NLO) pQCD calculations for the π^0 meson fail to describe the data with increasing energy. It could be expected that the deviation between data and calculation will continue with 8 TeV. But with an additional reference it could be possible to make better assumptions about the energy dependence for the NLO calculations and improve them.

1.5 Photon Interaction with Matter

The π^0 meson decays into two photons which have to be detected in the experiments. Photons themselves are massless, electrically neutral and show a constant velocity in the vacuum. They interact with the material they pass in three possible ways with a cross section depending on the energy they have. Those possibilities are either the *photoelectric effect, Compton scattering* or *pair creation* [13] and their energy dependent cross section can be seen in Figure 4.

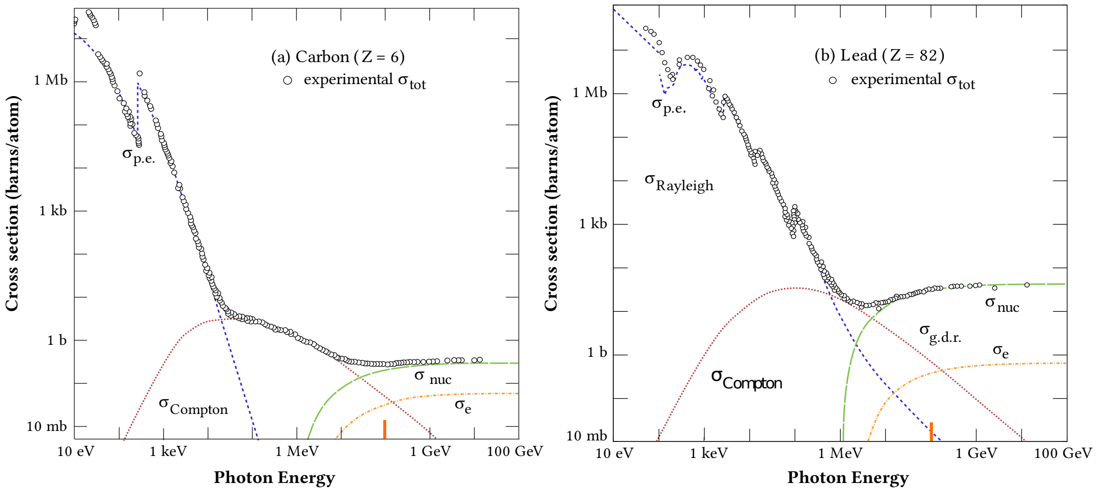

Figure 4: Cross sections for photons in carbon (**left**) and lead (**right**) for the different interaction processes in the materials. The cross sections are: $\sigma_{\mathrm{p.e.}}$ - Photoelectric effect (blue dashed line), $\sigma_{\mathrm{Compton}}$ - Compton scattering (red dotted line), σ_{nuc} - Pair production in nuclear field (green line), σ_{e} - Pair production in electron field (orange line). The orange line at around 100 MeV indicates the starting point in this analysis. Adapted from [13].

Photoelectric Effect

At low energies < 100 keV the photoelectric effect dominates, where an electron of the material absorbs the photon and can therefore be ejected from the atom it was originally bound to. In this case the electron receives all the energy the photon had ($E_\gamma = h\nu$) which leads to a kinetic energy of the electron of

$$E_{\mathrm{kin,e^-}} = E_\gamma - E_b \tag{6}$$

with E_b being the binding energy of the electron. Only if $E_\gamma > E_b$ the electron will be ejected from the atom.

Compton Scattering

At intermediate energies up to a couple of MeV the dominant process is Compton Scattering. This scattering process leads to a small energy transfer from the photon to an electron of the medium, which leads to a deflection of the photon under an angle θ from its original direction. As this process allows all possible angles after the deflection, the energy of the photon after the scattering process E_γ^* strongly depends on θ and can be calculated with

$$\frac{1}{E_\gamma^*} - \frac{1}{E_\gamma} = \frac{1}{m_e c^2} \cdot (1 - \cos\theta) \tag{7}$$

where the energy of the photon before the scattering is E_γ, the mass of the electron is m_e and c represent the speed of light.

Pair Production (Photon Conversion)

With energies above ≈ 1.02 MeV, the photon is able to create an electron-positron pair within the Coulomb field of an atom. Due to a small energy transfer to the nucleus the energy and momentum can be conserved in this process. With increasing energies the opening angle between the electron and positron gets narrower as the pair has to conserve the momentum of the initial photon. With higher energies the pair creation becomes the most dominant process which allows to make an approximation for the differential cross section for this interaction. [13]

$$\frac{\mathrm{d}\sigma}{\mathrm{d}x} = \frac{A}{X_0 N_A}\left[1 - \frac{4}{3}x(1-x)\right] \tag{8}$$

Here N_A stands for the Avogadro number and x or $(1-x)$ are the energies transferred to the electron and positron. The atomic number of the material is A and X_0 represents the radiation length which is the length after which an electron loses all but $1/e$ of its energy.

An integration of this differential cross section leads to the total e^+e^- cross section for high energies:

$$\sigma_{\mathrm{pair}} = \frac{7}{9}\frac{A}{X_0 N_A} \tag{9}$$

There is a certain probability for a photon to convert in the medium it traverses. This probability depends on the thickness x and the radiation length X_0 of the medium and can be expressed as:

$$P = 1 - \exp\left(-\frac{7}{9}\frac{x}{X_0}\right) \tag{10}$$

If a photon converts within the medium the conversion products (e^+e^-) have a chance to emit an additional photon due to bremsstahlung. This can lead to cascades in the material where pair creation and bremsstahlung alternate and expand over a large area. Pair creation is due to its dominance in high energies the most important process in the LHC experiments.

1.6 Electron Interaction with Matter

As pair creation is the dominant process in the LHC experiments, the interaction of the conversion products, the electrons and positrons, with the matter is as important as the photon interaction. For the electrons (positrons) there are two dominant processes for energy loss, *ionization* and *bremsstrahlung* which depend on its energy. At low energies the ionization is the dominant process and it can be described by a modified Bethe-Bloch formula [13]:

$$-\frac{\mathrm{d}E}{\mathrm{d}x} = Kz^2\frac{Z}{A}\rho\frac{1}{\beta^2}\left[\frac{1}{2}\ln\frac{2m_ec^2\beta^2\gamma^2T_{\max}}{I^2} - \beta^2 - \frac{\delta}{2}\right] \tag{11}$$

with $\frac{K}{A} = \frac{4\pi N_A r_e^2 m_e c^2}{A}$, $T_{\max} \approx 2m_ec^2\beta^2\gamma^2$ and the classical electron radius $r_e = \frac{e^2}{m_ec^2}$. Here N_A again stands for the Avagadro constant, A for nuclear protons, $\beta = v/c$ for the velocity of the electron and I for the mean ionization potential of the medium. As seen, the energy loss depends mostly on Z and β, while for small β it is proportional to $1/\beta$ and for higher energies it rises logarithmically.

As seen in Figure 5 the primary loss of energy at low energies is ionization, but also other processes (Møller scattering, Bhabaha scattering and e$^+$ annihilation) contribute in this energy region.

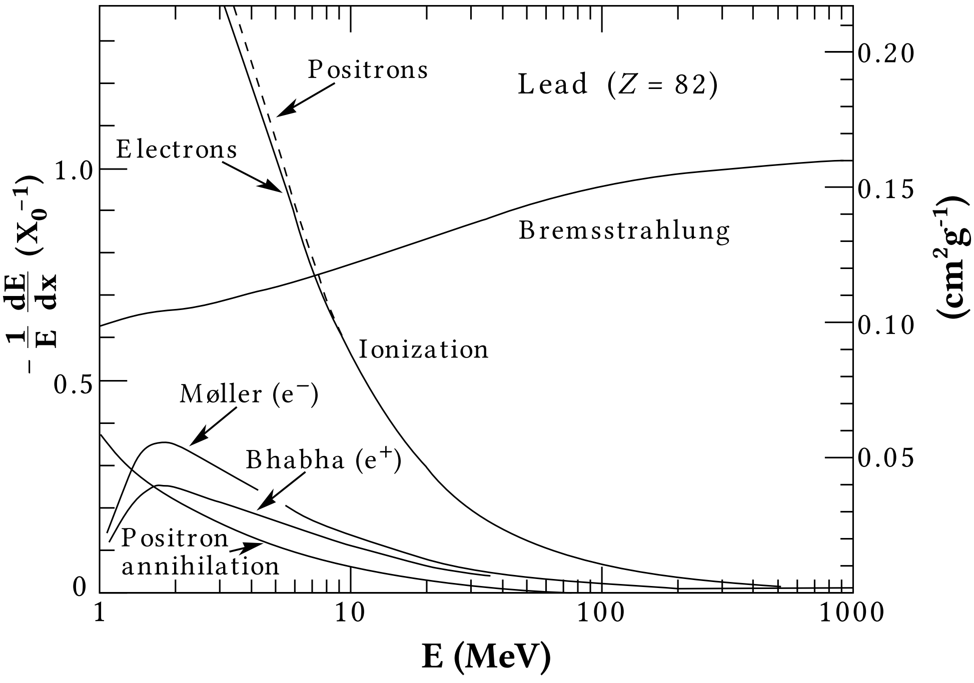

Figure 5: Fractional energy loss in lead for electron and positron as a function of their respective energy.[42]

Above a few tens of MeV bremsstrahlung dominates the energy loss as it nearly linearly rises compared to the logarithmic rise of the ionization loss. The electron there looses momentum due to the interaction with the field of a nuclei which leads to the irradiation of a photon and the energy loss due to bremsstrahlung [13] can be described by

$$-\frac{\mathrm{d}E}{\mathrm{d}x} = 4\alpha N_A \frac{Z^2}{A} r_e^2 E \ln \frac{183}{Z^{1/3}} = \frac{E}{X_0} \tag{12}$$

As seen in the formula there is a linear energy dependence of the energy loss and also a dependence of the radiation lengths.

1.7 The LHC Experiment

The Large Hadron Collider (LHC) at the European Organization for Nuclear Research (CERN) in Geneva on the Franco–Swiss border is currently the largest and most powerful particle accelerator in the world. It started operating on 10 September 2008 with the first proton beams in the main ring. With maximum center of mass energies of $\sqrt{s} = 14$ TeV and a peak luminosity of $L = 10^{34}$ $\mathrm{cm}^{-2}\mathrm{s}^{-1}$ for proton-proton collisions or $\sqrt{s_{\mathrm{NN}}} = 5.5$ TeV and $L = 10^{27}$ $\mathrm{cm}^{-2}\mathrm{s}^{-1}$ per nucleon-nucleon pair for lead-lead collisions it is about seven times more powerful than any other collider. The LHC was built inside the tunnel of the Large Electron Positron Collider (LEP) which has a circumference of 26.7 km and is on average 100 m under ground. Inside the tunnel the LHC holds two beam pipes which intersect at four points and contain particle beams traveling in opposite directions.

The protons for the beams are created by stripping away the electrons from a hydrogen atom. For the injection of the proton or lead beams the LHC uses a chain of pre-accelerators. In Figure 6 the injection chain is shown. It consists of the Linear Accelerators (LINACS), the Proton Synchrotron Booster (PSB), the Proton Synchrotron (PS) and the Super Proton Synchrotron (SPS) to allow the particle bunches to enter the LHC with an energy of 450 GeV where then they are accelerated to their full energy of 7 TeV or intermediate steps. A total amount of 1232 superconducting dipole magnets are used to keep the beam on its circular orbit with a radius of about 4 km. Those magnets can generate a field of 8.36 T while being cooled down to 1.9 K during operation.

There are four experiments located at the intersection regions of the LHC which can also be seen in Figure 6. Each experiment looks at a different kind of physics and for that the detectors are designed to focus on different characteristics of the collisions.

- **A** **T**oroidal **L**HC **A**pparatu**S** (**ATLAS**) is designed to observe particles at high transverse momenta and is a general purpose detector. It is one of the two LHC experiments involved in the Higgs boson discovery in 2012 and is continuing to make improved measurements to confirm the standard model or give possible clues for new theories in high energy physics. Additionally, the experiment investigates charge parity (CP) violation, super symmetries, additional dimensions and physics beyond the Standard Model.[23]

- The **C**ompact **M**uon **S**olenoid (**CMS**) experiment is, like the ATLAS detector, a general purpose detector at the LHC. It also searches for the Higgs boson and investigates extra dimensions as well as particles that could make up dark matter but with different detector techniques than ATLAS.

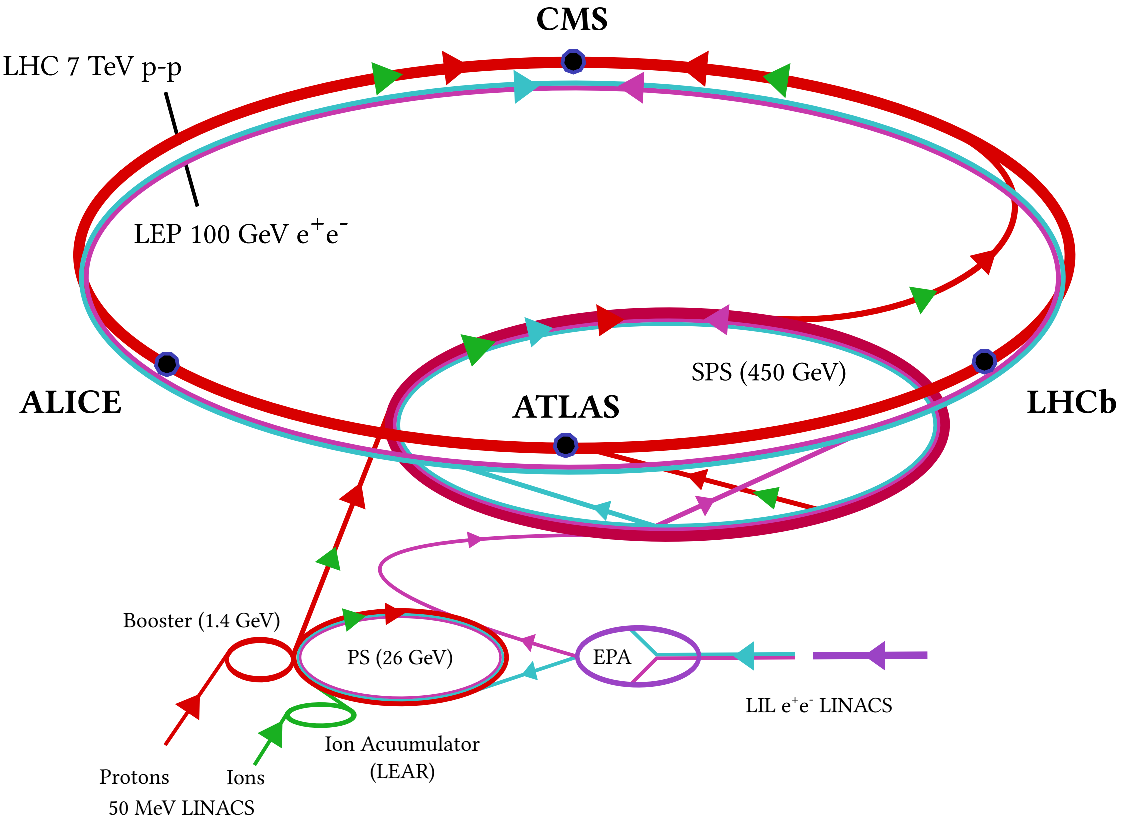

Figure 6: LHC and LEP injection scheme with the necessary pre-accelerators for proton-proton, heavy ion and electron-positron collisions.

- The **LHC b**eauty experiment (**LHCb**) is dedicated to investigate hadron decays which contain bottom or charm quarks. In addition the LHCb experiment measures CP violation. The studies also investigate the matter-antimatter asymmetry in the universe which the Standard Model does not describe completely.[24]

- **A L**arge **I**on **C**ollider **E**xperiment (**ALICE**) is the detector dedicated to heavy ion measurements at the LHC because it can handle high multiplicities, which occur in heavy ion collisions, with good particle identification (PID). The main task of the ALICE detector is to study the QGP. The next section will provide a more detailed view on ALICE.[22]

1.7.1 The ALICE Detector

The ALICE detector and its main components can be seen in Figure 7. It is divided into two subsystems: the central barrel and the forward muon spectrometer. The large red solenoid magnet from the L3 experiment at LEP is used to generate a magnetic field of 0.5 T for the central barrel detectors. The forward muon spectrometers are aligned outside of the solenoid and are placed behind thick layers of absorbing material. Going from the inside to the outer layer of the central barrel we have the Inner Tracking System (ITS), the Time Projection Chamber (TPC), the Transition Radiation Detector (TRD), Time-Of-Flight detector (TOF) and High Momentum Particle Identification Detector (HMPID) as well as two electromagnetic calorimeters the Photon Spectrometer (PHOS) and the

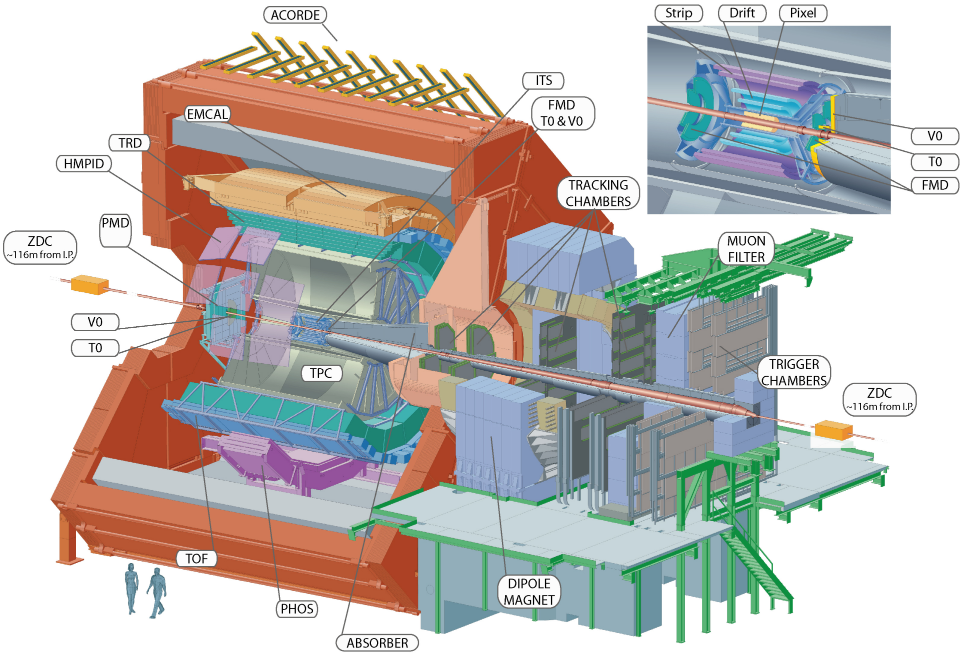

Figure 7: Overview of the detectors of the ALICE experiment. The inner barrel is embedded in the red solenoid while the forward muon spectrometers are placed further along the beam axis. [6]

Electromagnetic Calorimeter (EMCal). An overview of the different detectors and their acceptance in η and ϕ is given in Table 1.

Inner Tracking System (ITS)

The innermost detector, the ITS [5], extends from 3.9 to 43 cm and consists of six layers of silicon detectors which cover a pseudorapidity range of $|\eta| < 0.9$ which is equal to $\pm 45°$ relative to the interaction plane. The six layers of the ITS are a combination of two Silicon Pixel Detector (SPD), two Silicon Drift Detector (SDD) and two Silicon Strip Detector (SSD). Its main purpose is to reconstruct the primary vertex with more than 100 μm precision and to reconstruct secondary vertices from short living particles. Additionally it can identify particles with $p_{\mathrm{T}} < 200$ MeV/c which do not reach the outer detectors and improves the momentum and angular

Detector	η acceptance	ϕ acceptance	position	main purpose
ITS				
SPD 1(2)	±2 (±1.4)	full	$r = 3.9$ (7.6) cm	tracking, vertex
SDD	±0.9	full	$r = 15.0$ (23.9) cm	tracking, PID
SSD	±1	full	$r = 38$ (43) cm	tracking, PID
TPC	±0.9	full	$85 < r/\mathrm{cm} < 247$	tracking, PID
TRD	±0.8	full	$290 < r/\mathrm{cm} < 368$	tracking, $\mathrm{e}^{\pm}$ id
TOF	±0.9	full	$370 < r/\mathrm{cm} < 399$	PID
PHOS	±0.12	$220° < \phi < 320°$	$460 < r/\mathrm{cm} < 478$	photons
EMCal	±0.7	$80° < \phi < 187°$	$430 < r/\mathrm{cm} < 455$	photons and jets
HMPID	±0.6	$1° < \phi < 59°$	$r = 490$ cm	PID

Table 1: Different detectors of the ALICE experiment and their function [5].

resolution of the TPC by reconstructing particles from TPC dead areas.

Time Projection Chamber (TPC)

The TPC [31] serves as the main tracking system with good performance even in high multiplicity events with up to 8000 particles per rapidity unit. The detector extends from -2.5 m to 2.5 m in z-direction and therefore covers $|\eta| < 0.9$. Additionally it is able to measure over a large transverse momentum range of $0.05\ \mathrm{GeV}/c \leq p_\mathrm{T} \leq 100\ \mathrm{GeV}/c$ by using the energy loss of charged primary particles traversing its gas volume which is a mixture of Ne-CO_2-N_2 (90-10-5%). Due to drift times of about 90 μs of the electrons in the large chamber of the TPC, it happens that at high luminosity and therefore at high interaction rate, tracks of up to 30 events overlap in the detector. [7, 12]

Transition Radiation Detector (TRD)

The TRD consists of 540 large area drift chambers with the drift direction perpendicular to the wire planes. The transition radiation photons are absorbed by a Xe based gas mixture. [5, 43] It provides the separation of electrons and pions over a large momentum range above 1 GeV/c by analyzing the energy loss and transition radiation from particles traversing multiple layers with different dielectric materials. Additionally it is used for triggering on electrons and jets in pp and heavy ion collisions.

Time-of-Flight Detector (TOF)

By using Multigap Resistive Plate Chamber (MRPC), the TOF can measure particle flight times with a resolution of $\sigma_t \approx 120$ ps and therefore measures the velocity β of the particles. By combining the time of flight with the measured track length and the momentum information from tracking, the TOF allows to calculate the mass of the particle.

Electromagnetic Calorimeter (EMCal)

The EMCal [25] is located in the central barrel of ALICE and covers an angle of $\Delta\phi = 107°$ and a pseudorapidity range of $|\eta| < 0.7$. It consists of 12288 towers of layered Pb-scintillator with each tower containing 77 layers. The detector is located at 430 cm from the interaction point and able to measure neutral particles and the energy deposit of charged tracks. It was designed for focusing on the full reconstruction of jet quenching. In addition EMCal can be used as a fast trigger for jets, photons and electrons. EMCal The detector covers 107 degrees in azimuth and $|\eta| < 0.7$ in pseudorapidity

1.7.2 The ALICE Trigger System

The interaction rate in the ALICE detector is about a thousand times smaller than in ATLAS or CMS. This and the fact that some detectors have a long readout time is the reason for the three trigger levels used in the ALICE Trigger System (TRG) which are all part of the Central Trigger Processor (CTP). The first level of these triggers, the Level 0 (L0) trigger makes its decision ~0.9 μs after the collision using V0, T0, EMCal, PHOS and the Muon Trigger (MTR) [5]. The Level 1 (L1) trigger further evaluates the L0 events as part of the CTP algorithm and makes its decision ~6.5 μs (260 LHC clock cycles) after

L0. The huge latency is caused by two factors: the propagation times (e.g. Zero Degree Calorimeter (ZDC) with 113 m from the interaction point) and the computation times of the electronics from TRD and EMCal. L0 and L1 are responsible for triggering the electronics to buffer the event data for further analysis. The final trigger, the Level 2 (L2) trigger takes about 100 μs as it has to wait for the TPC drift times and triggers the sending of the event data to the computers of the Data Acquisition (DAQ) system. An overview of the triggers that provide input to the trigger decision is provided in Table 2.

detector	function	level
SPD	hit-multiplicity based trigger and hit-topology based trigger	L0
TRD*	electron trigger, high-p_{T} particle trigger, charged-jet trigger	L1
TOF	multiplicity trigger, topological (back-to-back) trigger, cosmic-ray trigger	L0
PHOS	photon trigger	L0
EMCal*	photon trigger, neutral-jet trigger	L0
ACORDE	cosmic-ray trigger (single and multiple hits)	L0/L1
V0*	coincidence based minimum-bias interaction trigger, centrality trigger	L0
T0*	event-vertex selection trigger, interaction trigger	L0
ZDC	minimum-bias interaction and electromagnetic-dissociation triggers in Pb-Pb	L1
MTR	single-muon trigger, dimuon trigger	L0

Table 2: Different triggers of the ALICE detectors and their function [5]. The triggers marked with a star (*) will be used in the trigger analysis in Chapter 4.

The CTP uses information about the LHC filling scheme [38] to suppress background while taking data. This task becomes more and more difficult since the number of bunches and the bunch spacing was changed drastically during the past three years. A detailed look at the influence of different triggers on the statistics, especially at high p_{T}, will be given in chapter 4.

1.7.3 The Software Framework

To be able to work with the data provided by the detectors the ALICE experiment uses a powerful software framework, called AliRoot [41], which includes a variety of tools for simulation, reconstruction and physics analysis of the data. The framework itself is based on ROOT [49] which is based on object-oriented programming in C++. It is developed and continously improved at CERN to provide the best possible data analysis. [16]

Also Monte Carlo generators are included in the AliRoot framework, for example PYTHIA8 [53] and PHOJET [28] which are used for full-event and single-particle generation. This is useful as the generators provide full kinematic information and the origin of each particle. The interaction of those simulated particles with the detector while traveling through its material is simulated with GEANT3, GEANT4 or FLUKA.

In addition, afterburners are used to make particle correlations. They modify the multi-particle momentum distributions by changing the momenta of the particles produced by another generator. [5]

2 Data Analysis with the Photon Conversion Method

In this chapter the Photon Conversion Method (PCM) is explained. For this, the datasets from the experiment and Monte Carlo (MC) simulations which are used for the pion analysis will be introduced.

2.1 Data Sets and Quality Assurance

In this analysis proton-proton (pp) collision data from data taking in 2012 at a collision energy of $\sqrt{s} = 8$ TeV will be used [50]. The data itself is split into periods (LHC12[a-i]), where each period is about one month of data taking and is further divided into multiple runs.

2.1.1 Event Selection for the 2012 Data

In this analysis the default minimum bias trigger is the V0AND (kINT7) trigger. This trigger setup allows to inspect an invariant cross-section of (55.74 ± 0.46) μb [10]. In addition, only those events are considered which have a reconstructed primary vertex with $|z_{\mathrm{vtx}}| < 10$ cm to the center of the ALICE central barrel. To reconstruct this vertex, global tracks or only SPD tracklets can be used, as long as they have at least one contributing track or tracklet to the vertex [17]. Table 3 shows the statistics of the data samples for the analysis including the total number of events and the integrated fraction of events being lost due to the different vertex conditions. Moreover Figure 8 (top) and Figure 28 (top) in the appendix show the run dependence of these numbers. The spectra are normalized with the following number of events where N_{MB} is the number of minimum bias events triggered with V0AND:

$$N_{\mathrm{norm,evt}} = N_{\mathrm{MB,Vtx},|z_{Vtx}|<10\mathrm{cm}} + \frac{N_{\mathrm{MB,Vtx},|z_{vtx}|<10\mathrm{cm}}}{N_{\mathrm{MB,Vtx},|z_{vtx}|<10\ \mathrm{cm}} + N_{\mathrm{MB},Vtx,|z_{vtx}|>10\mathrm{cm}}} N_{\mathrm{MB,no\ Vtx}} \tag{13}$$

In ALICE the limiting factor for the data taking rate is the TPC. Due to long drift times for the electrons in the chamber, events can overlap and create pile-up. To avoid this factor, ALICE has to reduce the interaction rate by displacing both beams. This has become more and more important as the delivered instantaneous luminosity from the LHC has been constantly increasing since 2009. In this analysis a pile-up rejection is therefore included which removes events that have more than one vertex reconstructed based on SPD tracklets. Compared to previous periods at lower energies, the pile-up rejection becomes even more important in the $\sqrt{s} = 8$ TeV periods as the number of bunches was drastically increased and the bunch spacing was reduced by a factor of 4-10 compared to the previous 2.76 TeV runs. The detailed run dependent fraction of rejected events due to in-bunch pile-up can be seen in Figure 27 and the out-of-bunch pileup correction will be discussed in 3.1.2.4.

A list of runs used for the analysis can be found in Table 13. For the analysis the runs 179569, 179584,179585 and 179591 from period LHC12c are not taken into account due to missing SDD signals. Additionally the runs 185697, 185698, 185699 and 186701 are excluded due to noisy SSD modules in layer 6 and run 192778 due to SSD layer 5

Data Set	Events for normalization N_{norm}	Min. Bias. Events (MB) N_{MB}	$\frac{\text{MB+Vtx+}\lvert z_{vtx}\rvert\text{<10}}{\text{MB}}$	$\frac{\text{MB+Vtx+}\lvert z_{vtx}\rvert\text{>10}}{\text{MB}}$	$\frac{\text{MB+ no Vtx}}{\text{MB}}$	$\frac{\text{MB+Pile-up}}{\text{MB}}$
Data						
LHC12a	1.36e07	1.50e07	0.89	0.073	0.018	0.012
LHC12b	9.65e06	1.07e07	0.89	0.088	0.013	0.008
LHC12c	3.97e06	4.41e06	0.89	0.084	0.012	0.008
LHC12d	9.49e06	1.03e07	0.91	0.074	0.012	0.008
LHC12e	3.45e06	3.81e06	0.90	0.077	0.007	0.015
LHC12f	7.82e06	8.72e06	0.88	0.098	0.019	0.006
LHC12g	4.70e06	5.30e06	0.87	0.100	0.019	0.005
LHC12h	3.87e07	4.21e07	0.91	0.064	0.010	0.013
LHC12i	1.95e06	2.13e06	0.91	0.061	0.004	0.024
MC						
LHC14e2a	3.86e07	4.20e07	0.86	0.076	0.065	0.000
LHC14e2b	3.84e07	4.17e07	0.92	0.081	0.000	0.000
LHC14e2c	3.72e07	4.07e07	0.91	0.081	0.005	0.000

Table 3: Number of events used for normalization in the analysis for each period. In addition the number of events of the V0AND Minimum Bias trigger and the fractions for $\frac{\text{MB+Vtx+}\lvert z_{vtx}\rvert\text{<10}}{\text{MB}}$, $\frac{\text{MB+Vtx+}\lvert z_{vtx}\rvert\text{>10}}{\text{MB}}$, $\frac{\text{MB+ no Vtx}}{\text{MB}}$ and $\frac{\text{MB+Pile-up}}{\text{MB}}$ for each period used in the analyis.

charge problems.

The mean number of primary tracks in the TPC and the measured fraction of photon candidates per event as a function of run number are shown in Figure 8 (middle and bottom) and more detailed in the appendix in Figure 8.

2.1.2 Monte Carlo Simulations for pp Collisions

As some corrections to the spectra from the data will be necessary, two different Monte Carlo event generators are used as input for a full detector simulation:

Pythia 8

The Pythia event generator [52] uses Leading Order (LO) QCD matrix elements with the initial and final state parton showers to generate hard parton-parton interactions. In addition diffractive processes based on the Regge Field Theory are used to better reproduce the data [8]. Pythia can be used to generate high-energy events from collisions between elementary particles such as e^+, e^-, p and $\overline{p}$ in every possible combination as well as string fragmentation and decay. As the QCD calculation doesn't hold for low p_{T} of the partons from the hard interaction, a lower cut-off with $p_{\text{T}} > 2$ GeV is used to make a connection between low and high momentum processes. The LUND String Model is the basis for the hadronization simulations and for the decays, the decay properties from [13] are used and the hadrons are decayed according to the decay table.

Phojet

The Phojet Monte Carlo event generator is based on the two-component Dual Parton

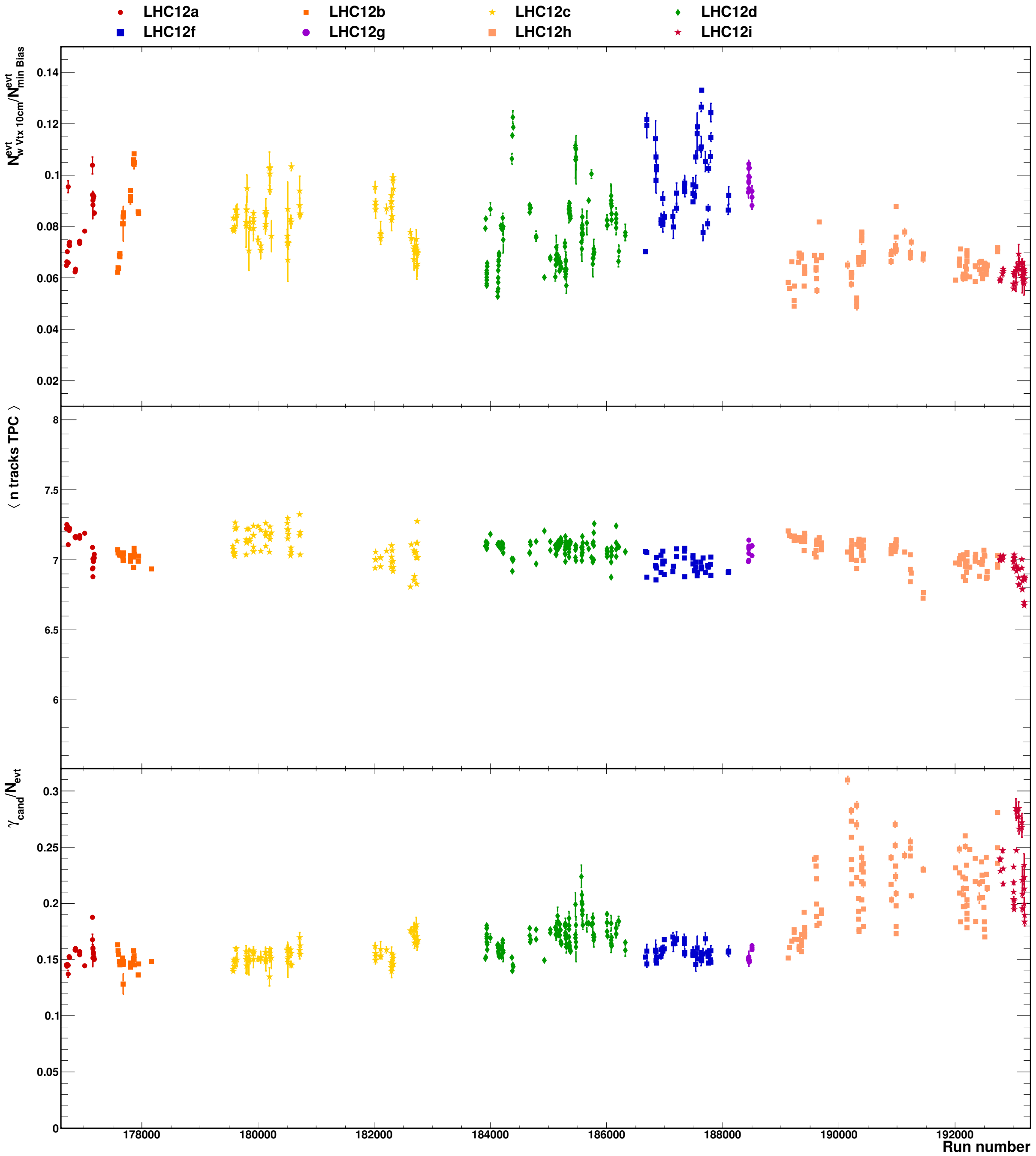

Figure 8: Top: Fraction of events rejected due to a vertex position outside $Z_{\text{vtx}} = \pm 10$ cm with respect to the total number of collected minimum bias events in the respective run. **Middle**: Mean number of primary tracks reaching the TPC versus run number for the different pp data samples. **Bottom**: Fraction of photon candidates in pp events normalized to the number of events, which fullfill the event selection criteria.

Model (DPM) [20] and includes soft hadronic processes, which are described by the supercritical Pomeron, and hard processes, which are described by pertubative constituent scattering. This allows the model to describe hadron-hadron, photon-hadron and photon-photon interactions at high energies [29]. A p_{T} cutoff at ≥ 3 GeV is made for the calculation of the hard processes while the soft interaction uses a model of multiple strings that are stretched between the proton and the resolved hadronic state of the photon. The characteristic features of this model are multiple soft and hard interactions [9]. The multiplicities of those interactions are calculated using a unitarization scheme [11] which was tuned to make the sum of the hard and soft cross sections nearly independent of the p_{T} cutoff.

2.2 TPC Single Sector Photons

As part of the Quality Assurance (QA) of the data a more detailed study of the TPC data has been taken. The following calculations aim to distinguish photons and their conversion products which are crossing only one sector of the TPC from the rest of the photons. The restriction that none of the conversion products crosses the border to another sector is important as we want to get information about the Inner Readout Chamber (IROC) and the Outer Readout Chamber (OROC). Both experienced voltage changes during data taking which could have influenced the measurements. The single sector photons could be used to check for these influences.

2.2.1 Coordinate System

The following basic guidance is taken from the ALICE TPC Numbering Conventions[14].

- The origin of the coordinate system (0,0) is at the beam interaction point.
- The x-coordinate is horizontal and perpendicular to the beam direction. Positive x is pointing towards a vertical line through the accelerator center.
- The y-coordinate is perpendicular to the x-axis and to the beam direction. It is pointing upward with an angle of 3.5875 mrad with respect to the vertical.
- The z-coordinate is parallel to the beam direction. (Will not be considered here.)
- The ϕ-coordinate increases counter-clockwise from the x-axis ($\phi = 0$) to the y-axis ($\phi = \frac{\pi}{2}$) looking from the shaft side towards the muon side.
- The Inner Readout Chamber (IROC) has the following dimensions:
  - distance from the center to the bottom of the first pad row 848.5 mm
  - distance from the center to the top of the last pad row 1321 mm
- The Outer Readout Chamber (OROC) has the following dimensions:
  - distance from the center to the bottom of the first pad row 1346 mm
  - distance from the center to the top of the last pad row 2466 mm

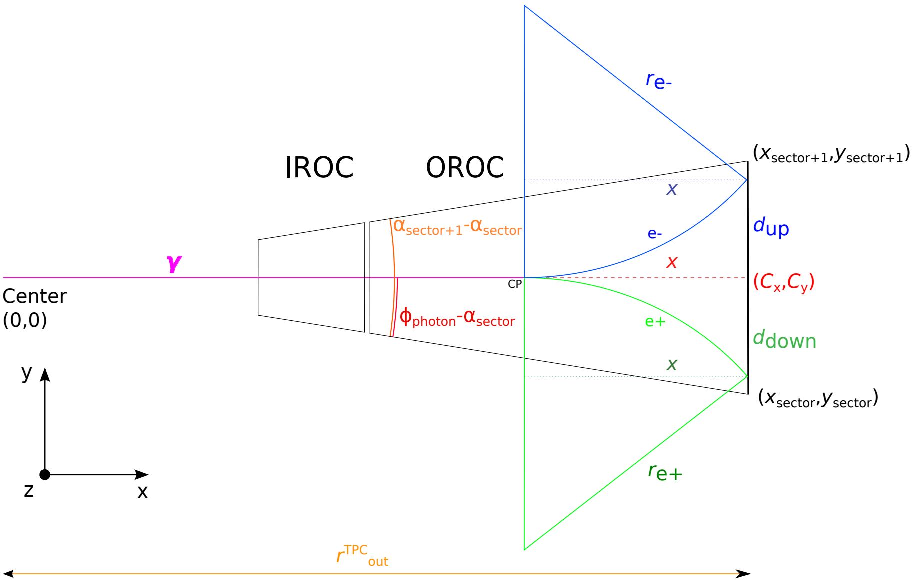

Figure 9: Overview of the single sector photon reconstruction with a visualization of the parameters used in the calculations. The black lines represent the outline of one TPC sector (IROC and OROC), in magenta the flightpath of the photon, in blue the electron parameters and in green the position parameters.

2.2.2 Calculation

To find the photons and their conversion products that only cross one sector we have to make different assumptions and cuts. The geometry of the reconstruction can be seen in Figure 9.

The conversion point R_{conv} should be between 5 cm and 180 cm from the beam interaction point. The angle of the photon with respect to the x-axis should be within the angular range of one TPC sector ($\alpha_{\text{sector}} = \frac{\pi}{9} \equiv 20°$) with the sector number N_{sector}.

$$\alpha_{\text{sector}} \cdot N_{\text{sector}} < \phi_{\text{photon}} < \alpha_{\text{sector}} \cdot (N_{\text{sector}} + 1)$$

Due to the Lorentz force on charged particles of transverse momentum p_{T} in GeV$/c$ within the magnetic field of B $=$ 0.5T, the electron and positron will be on a circular trajectory with a transverse momentum dependent radius as soon as they are created. The radius of this trajectory in centimeter is given by:

$$r_{e+/-} = \frac{1}{eB} \cdot p_{\text{T}} = \frac{2000}{3} \cdot p_{\text{T}}$$

This radius must be greater than the remaining distance from the conversion point to the outer wall of the TPC ($r^{\text{TPC}}_{\text{out}} = 2466$ mm). Otherwise the particles would not be able to reach the outer wall.

$$x = r^{\text{TPC}}_{\text{out}} - R < r_{e+/-}$$

From this the deflection of the electron at the $r^{\text{TPC}}_{\text{out}}$ can be calculated:

$$d^{\text{max}}_{\text{e}+,-} = r_{e+/-} - \sqrt{r^2_{e+/-} - x^2}$$

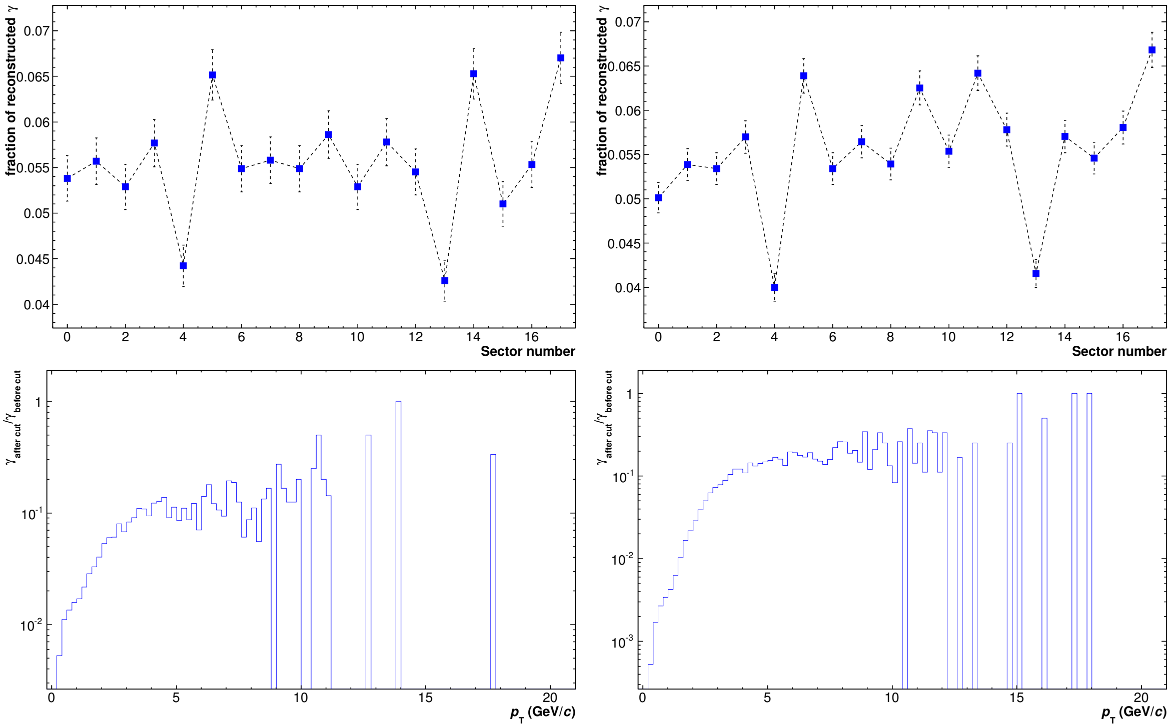

Figure 10: Photon candidates per sector normalized to the total number of photon candidates (**top**) and ratio of photons that survive the cuts compared to the total number of photons (**bottom**). Plots on the left side are from LHC11c and on the right side from LHC12c.

The photons continued flightpath creates the reference point on the outer TPC wall (C_x, C_y).

$$\begin{pmatrix} C_x \\ C_y \end{pmatrix} = \begin{pmatrix} \cos(\phi_{\text{photon}}) \cdot r_{\text{out}}^{\text{TPC}} \\ \sin(\phi_{\text{photon}}) \cdot r_{\text{out}}^{\text{TPC}} \end{pmatrix}$$

The final step is to check if this deflection is smaller than the remaining distance to the edge of the sector ($d_{\text{up,down}}$). For this we need the x and y coordinate of the sector edges $(x_{\text{sector}}, y_{\text{sector}})$:

$$\begin{pmatrix} x_{\text{sector}} \\ y_{\text{sector}} \end{pmatrix} = \begin{pmatrix} \cos(\alpha_{\text{sector}} \cdot N_{\text{sector}}) \cdot r_{\text{out}}^{\text{TPC}} \\ \sin(\alpha_{\text{sector}} \cdot N_{\text{sector}}) \cdot r_{\text{out}}^{\text{TPC}} \end{pmatrix}$$

$$d_{\text{down}} = \sqrt{(C_x - x_{\text{sector}})^2 + (C_y - y_{\text{sector}})^2}$$

$$d_{\text{up}} = \sqrt{(C_x - x_{\text{sector+1}})^2 + (C_y - y_{\text{sector+1}})^2}$$

To be sure that the electrons and photons are in the detector, a small safety distance from the sector border ~0.5 cm is used. Because of its negative charge and the orientation of the magnetic field the electrons will be deflected towards the upper edge of the sector and the positrons towards the lower edge. The magnetic field can also be inverted which leads to an inverse deflection of the electrons and positrons.

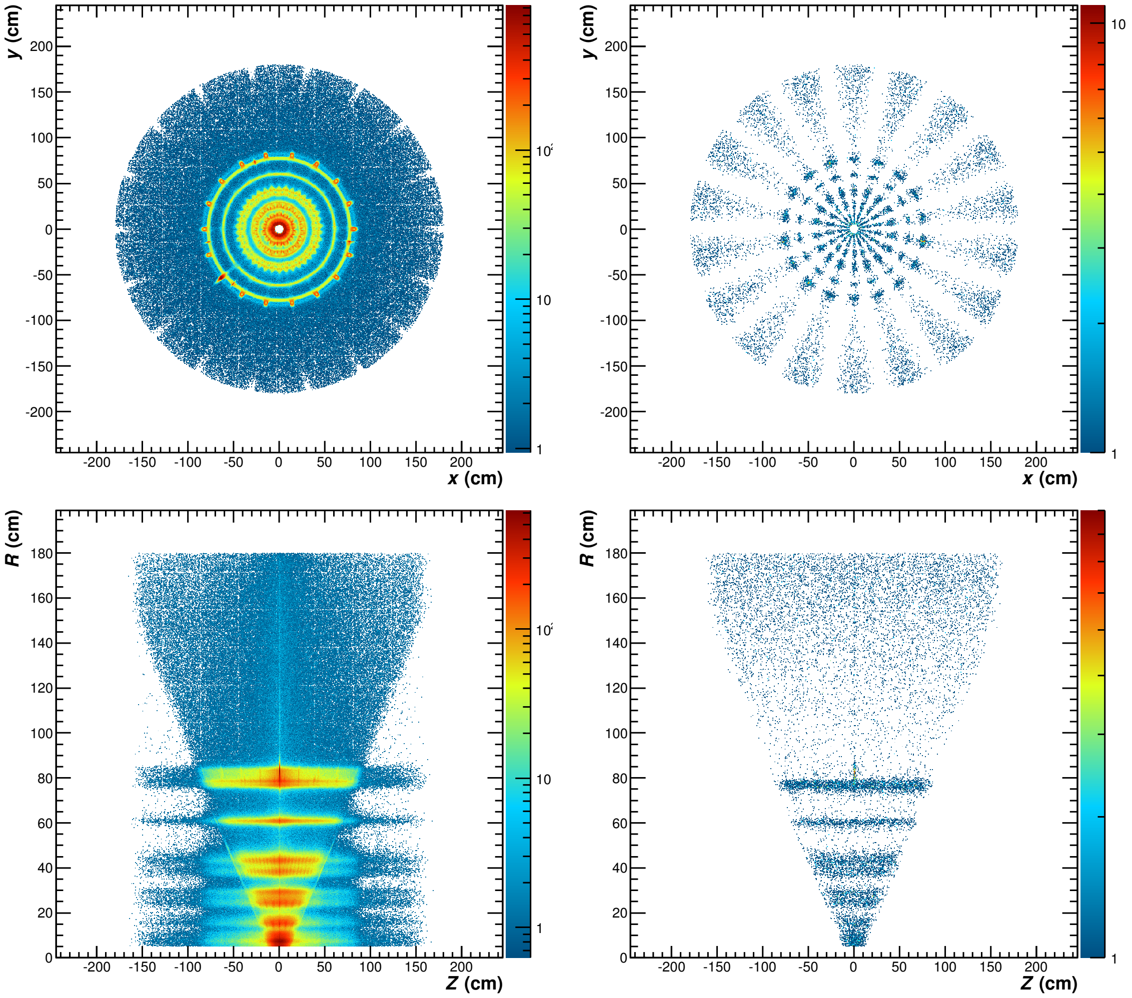

Figure 11: Comparison between the conversion points before and after the cuts in the X-Y plane (**top**) and in the Z-R plane (**bottom**). The detector symmetry is clearly visible (**left**) as well as the restriction to the 18 sectors after the cuts (**top right**). The cuts remove all conversion points that are outside a certain η range, therefore they act like a *line-cut* in the Z-R plane (**bottom right**). Data from LHC12c.

2.2.3 Photon Candidates per Sector

For the realization of these calculations a new macro was written which can be used in combination with the Quality Assurance output [1]. It produces multiple plots, where one is with photon candidates per sector. Figure 10 shows the output for two example periods (LHC11c and LHC12c) and therefore also for different beam energies. For both energies the distributions show a similar shape with two dips at S04 and S13 (see Figure 12 for the numbering of the sectors). Also visualized is the loss of statistics due to the cuts

---

[1] http://git.cern.ch/pubweb/AliRoot.git/blob/master:/PWGGA/GammaConv/AliAnalysisTaskConversionQA.cxx

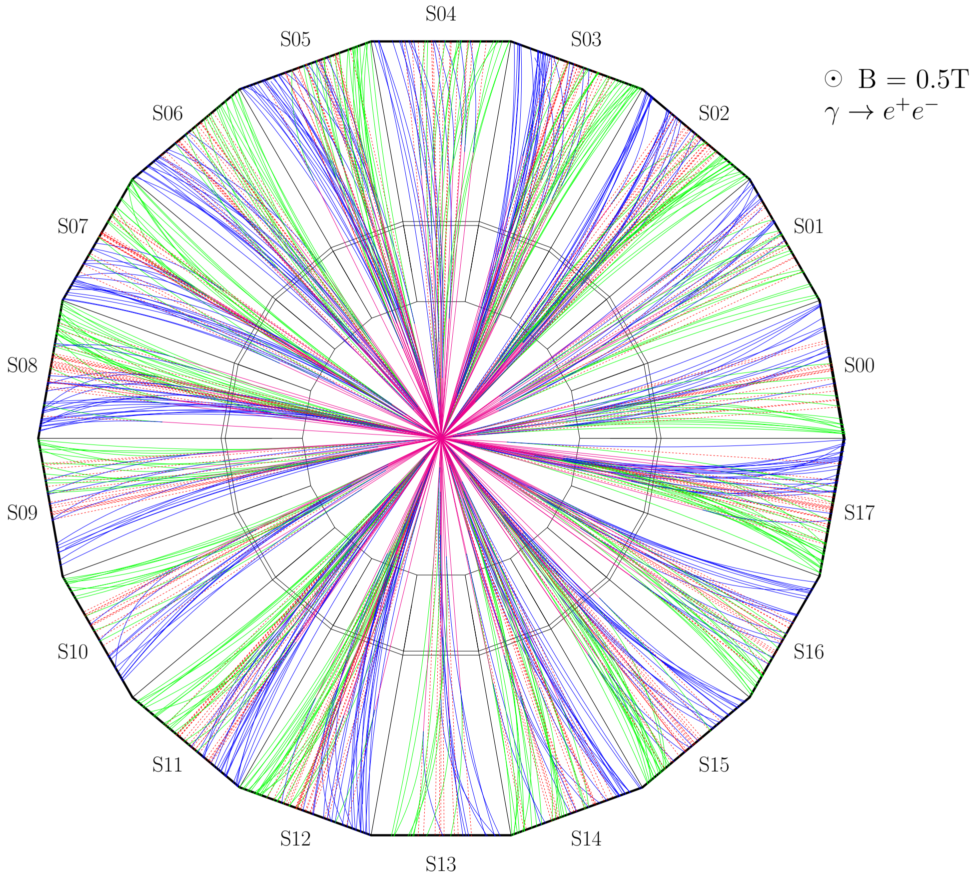

Figure 12: Visualization of the particle flightpaths and the correctness of the calculations. Photon flightpaths in magenta, electrons in blue and positrons in green.

and depending on p_T, the ratios of photons before and after cuts is plotted in Figure 10. With the cuts many of the low p_T photons are removed as they are most likely to cross the border to another sector. With increasing p_T the ratio levels out to about 30% of the initial photons and after all cuts only 1-2% of all photons remain as photon candidates for the analysis.

To show the influence of the cuts on the conversion points, in Figure 11 the conversion points in the XY and ZR plane are plotted before and after the cuts. In the XY plane the strong restriction to the conversions within one sector become visible and all 18 sectors are clearly separated. In the ZR plane one can see that the cuts that are used act like a line cut on an η range, which has not been applied yet for the QA output.

2.2.4 Cross-check of the Calculations

To check that the calculation was correct, the remaining photons, positrons and electrons are plotted on an ALICE TPC schematic grid in Figure 12. In this diagram the official naming convention for the TPC can be seen where the first sector is S00 at an angular range of $0° - 20°$. The photons flightpath is indicated in magenta until the conversion point and then continued by a dotted red line until the outer wall of the TPC. In the plot only a sample of 1800 photon candidates is plotted; electrons are shown in blue and positrons in green.

It can be seen that the calculation works perfectly and the remaining photon candidates and their conversion products only cross one sector of the TPC. With the help of this analysis it might be possible to see differences due to voltage changes in the IROC and OROC. Due to a lack of statistics it was not possible to validate this in the respective runs where such changes were made. But a closer analysis will be made in the future.

2.3 Photon Reconstruction and Selection

By using a secondary vertex finder [16] the converted photons can be reconstructed via their conversion products. The conversion point resolution can be improved by assuming that the momenta of the conversion products are parallel at the point of their creation and the spatial distribution of the conversion points will be shown in the next section in the XY and ZR-plane in Figure 11. For the photon selection different cuts will be applied. Those can be split into three categories, the track and V^0 selection, the electron identification, and the photon selection cuts. The different cuts will be discussed in the following subsections.

2.3.1 Track and V^0 Selection

Track and V^0 cuts	**Meson Analysis pp**
V^0 finder	On-the fly
minimum track p_T cut	$p_{T,\text{track}} > 0.05$ GeV/c
Cut on $\frac{N_{\text{clusterTPC}}}{N_{\text{findableclusters}}}$	$> 60\%$
Cut on R_{conv}	$5\text{cm} < R_{\text{conv}} < 180\text{cm}$
Cut on Z_{conv}	$\lvert Z_{\text{conv}}\rvert < 240$ cm
η cut	$\lvert\eta\rvert < 0.9$

Table 4: Standard cuts for the track and V^0 selection for the pp analysis

Table 4 shows an overview of the standard cuts for the analysis in terms of basic track and V^0 selection. The on-the-fly V^0 finder is taken as the standard V^0 finder type for this analysis as the tight cuts for the offline V^0 finder are not necessary.

After the V^0 candidates are selected, the secondary tracks have to fulfill several requirements. Those tracks are required to have no kink-topology, to fulfill the TPC refit condition and to have a minimum track p_T of 50 MeV/c. In addition the cut for more than 60% of all theoretically possible TPC clusters should guarantee a certain track quality.

There is also a cut on the photon pseudorapidity η which is interpreted as the angle between the beam-axis and the orientation of the 3-momentum vector of the particle in the ZR-plane. This cut however does not take the starting point of the particle into account and therefore we would get photon candidates which are outside the angular dimensions of the detector. By using a line-cut, which represents a cut on the geometrical η distribution of the conversion points with the nominal center of the detector as origin, it is possible to exclude those additional candidates. The cut is made by using the following condition:

$ZR_{\text{Slope}} = \tan(2 \times \arctan(\exp(-\eta_{\text{cut}})))$ and $Z_0 = 7$ cm while the coordinates of $R_{\text{conv}}, Z_{\text{conv}}$ are determined with respect to the center of the detector (X,Y,Z) = (0,0,0).

$$R_{\text{conv}} > |Z_{\text{conv}}| \times ZR_{\text{Slope}} - Z_0 \tag{14}$$

The cuts on R_{conv} and Z_{conv} are used to make sure that the reconstruction of secondary tracks is made inside the TPC and are therefore limited to $Z_{\text{conv}} < 240$ cm and $R_{\text{conv}} < 180$ cm. Additionally only those events with $R_{\text{conv}} > 5$ cm are considered to reduce the contamination from π^0 and η Dalitz decays.

2.3.2 Electron Identification Cuts

There are five different techniques to identify electrons in ALICE:

1. Energy deposition (dE/dx) in the ITS
2. Energy deposition (dE/dx) in the TPC
3. Time-of-flight measurement with the TOF
4. Transition radiation or energy loss in the TRD
5. Energy deposition in the calorimeters

For this analysis the most important measurement is the dE/dx in the TPC while the other techniques were not used as they show a significant loss in efficiency. The TPC signal still contains some contamination but this is not significant as a completely pure electron signal is not needed for the analysis. In Table 5 the cuts for the electron identification are shown which reduce influences from other particles due to a cut around the theoretical energy loss line.

Particle identification cuts	**Cut Range**
nσ_e TPC dE/dx	-3 < nσ_e < 5
nσ_π TPC dE/dx	n$\sigma_\pi > 2$ (0.4 GeV/c < p < 100 GeV/c)

Table 5: Standard cuts for the track and V^0 selection for the pp analysis

The most important cut for electron identification is a cut around the hypothesis for the electron energy loss in the TPC in terms of standard deviations ($n\sigma_e$) from this value. The cuts for the analysis are chosen to be very tight. This results in a increased pion rejection and the electrons are mostly uncontaminated from pions inside the remaining area.

Additionally, a cut on the pion nσ_{π^0} is used to exclude these pions. This cut is applied over the momentum range of 0.4 GeV/$c < p <$ 100 GeV/c and removes particles that are below 2 σ_π of the pion line.

In Figure 13 (top) the electrons before (left) and after (right) all electron PID and photon PID cuts can be seen. A small fraction of remaining pions, protons and kaons is still visible after the cuts, but the electron sample is clean enough for the analysis.

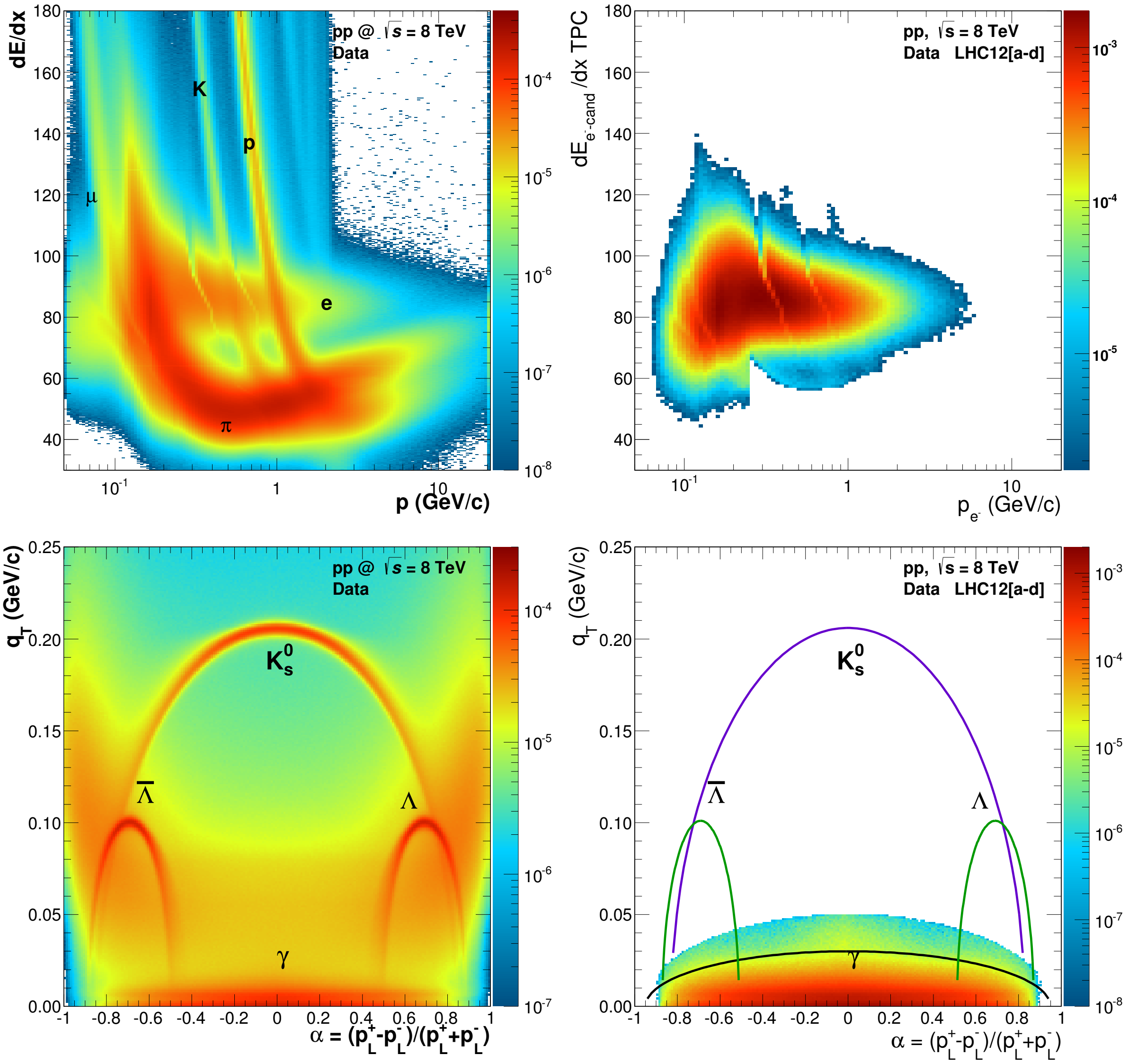

Figure 13: dE/dx plot (**top**) for the V0 daughters and Armenteros Podolanski plot (**bottom**) for the V0s before (**left**) and after (**right**) all electron and photon selection cuts.

2.4 Photon Selection

Photon cuts	**Cut Range**
χ^2_γ/ndf	triangular cut with χ^2_γ/ndf < 30 and $\Psi_{\text{Pair}} < 0.1$
q_{T}	elliptic cut with $q_T < 0.05$ GeV/c and $\alpha_\gamma = 0.9$

Table 6: Standard cuts for the photon selection for the analysis

With the cuts that were applied in the last section, mainly electrons from the V^0 were selected and the photon sample reaches a very high purity. This however can be further improved by restricting the photon mass and the opening angle between the reconstructed photon momentum vector and the vector joining the collision vertex and the conversion point.

To exclude K^0_S, Λ and $\overline{\Lambda}$ an elliptical cut in $q_{\text{T}} = p \times \sin\theta_{\text{mother-daugther}}$ and α of the Armenteros-Podolanski plot [46] is used. In this plot one can see the projection of the momentum of the daughter particle with respect to the mother particle in the transverse direction (q_{T}) versus the longitudinal momentum asymmetry ($\alpha = (p^+_{\text{L}} - p^-_{\text{L}})/(p^+_{\text{L}} + p^-_{\text{L}})$). If considered in the laboratory frame, the daughter particles of the photon fly in the same direction as the photon under a small opening angle. Therefore the q_{T} of the real photons is close to zero. The symmetry of the distribution in the Armenteros-Podolanski plot in Figure 13 (bottom) is due to the fact that the decay products have the same mass. A heavier particle however has a larger opening angle and therefore shows a larger q_{T}. This allows to use a cut in this q_{T} distribution and by that remove the contamination of K^0_S, Λ and $\overline{\Lambda}$ and therefore create a clean photon sample.

A two dimensional cut in χ^2/ndf and Ψ_{Pair} is used in addition to the q_{T} cut. The χ^2/ndf cut is applied on a fit of a generic particle decay model based on the Kalman filter method to a reconstructed V^0. For this V^0 it is assumed that the particle has no mass and comes from the primary vertex. The Ψ_{Pair} cut is based on the opening angle of the electron-positron pair from a photon conversion and the fact that the bending of the tracks in the magnetic field is small. Therefore a cut in Ψ_{Pair} can suppress remaining track combinations by limiting the ratio of the relative opening angle of the e^+e^- pair after creation to the opening angle at a distance of 50 cm from the conversion point. [4] In this analysis Ψ_{Pair} is limited to a maximum value of 0.1. The effects of the cuts can be seen in Figure 13 (bottom) with the distribution in the Armenteros-Podolanski plot before (left) and after (right) applying the cuts.

3 Neutral Pion Analysis

The neutral pion analysis including the systematic error estimation in pp collision at $\sqrt{s} = 8$ TeV will be discussed in this chapter. In the first section a general overview of the analysis method will be given and afterwards the results from $\sqrt{s} = 8$ TeV will be compared to published results from pp collision at three different center of mass energies ($\sqrt{s} = 7$, 2.76 and 0.9 TeV) [3, 4].

3.1 Neutral Pion Reconstruction

By combining photon candidates from the V^0 sample into pairs and excluding pairs with an opening angle of less than 5 mrad the invariant mass for each pair can be calculated with

$$M_{\gamma\gamma} = \sqrt{2E_{\gamma_1}E_{\gamma_2}(1 - \cos\theta_{12})} \tag{15}$$

where the energies of the two photons are given by $E_{\gamma_{1,2}}$ and the opening angle between them in the laboratory system by θ_{12}. The mass of the π^0 meson cannot be determined exactly with this method but in the invariant mass plot they appear as an excess at their respective mass, $m_{\pi^0} = 134,976$ MeV/c^2 for the π^0 [13]. This can be seen in Figure 14 in the invariant mass distribution for the photon pairs close to the π^0 meson rest mass. The π^0 can be distinguished from the background very well which allows the π^0 extraction at high and low p_{T}. As the background is put together with combinations of photon pairs the combinatorial background can be calculated with a special technique.

Event Mixing method With this method photons from different events are combined to remove any correlation between them. It was shown that the shape of the background depends on the event multiplicity. Also the primary vertex position in Z and the transverse momentum influence the shape. This is the reason why the photon candidates are binned in multiplicity and Z vertex position bins while it was tried to keep the same statistics in each bin. [1, 37]

3.1.1 Signal Extraction

For the meson signal extraction, the invariant mass distribution of the photon pairs is calculated in different p_{T} bins. The π^0 analysis ranges from a transverse momentum of 0.4 GeV/c reaching up to a maximum of 8 GeV/c. The plots for all the p_{T} bins can be seen in the appendix in Figure 30. The calculation is done once for photons from the same event and afterwards for photons from mixed events for background subtraction. To subtract the mixed event background distribution it needs to be scaled to the invariant mass distribution. This can be done either on the left or the right side of the peak, but has to be as close to the peak as possible without going into the peak itself. After the normalization, the background is subtracted from the signal. The resulting invariant mass distribution with signal and residual background for an example p_{T} bin can be seen in Figure 14. Then the signal after the subtraction is fitted with a Gaussian function combined with an exponential low-energy tail on the left side which accounts for electron bremsstrahlung. In addition there is a linear part that describes the remaining background if the combinatorial background does not describe the background under the peak. The fit function is given by:

$$y = A \cdot \left[G(M_{\gamma\gamma}) + \exp\left(\frac{M_{\gamma\gamma} - M_{\pi^0}}{\lambda} \right) (1 - G(M_{\gamma\gamma}))\theta(M_{\pi^0} - M_{\gamma\gamma}) \right] + B + C \cdot M_{\gamma\gamma} \tag{16}$$

$$\text{with } G = \exp\left[-0.5 \left(\frac{M_{\gamma\gamma} - M_{\pi^0}}{\sigma_{M_{\gamma\gamma}}} \right)^2 \right] \tag{17}$$

Here G represents a Gaussian function with the width σ, the amplitude A and the mean position M_{π^0}, which can be identified with the reconstructed mass position of the π^0 meson. The parameter λ represents the inverse slope of the exponential function which is set to zero by the Heavyside function $\theta(M_{\pi^0} - M_{\gamma\gamma})$ above M_{π^0}. The parameters of the linear function are given by B and C. In Figure 14 the mixed event combinatorial background is shown on the left side with the blue line and the peak fit on the right side with the cyan line.

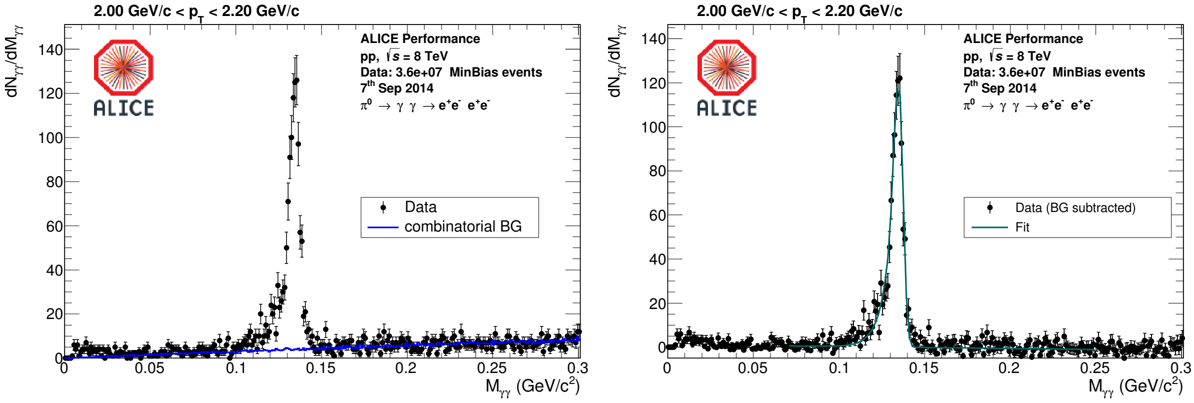

Figure 14: Invariant mass distribution for an example bin with the p_{T} range of 1.4 GeV/c to 1.6 GeV/c for π^0 with background (**left**) and without background (**right**). The data is plotted in black, the scaled combinatorial background is drawn in blue and the fit function for the π^0 mass peak in cyan.

From the fit one can get the invariant mass and the full width at half maximum (FWHM) of the meson in the respective p_{T} bin which can be seen in Figure 15. In addition to the 8 TeV values there are also the mass and the FWHM from lower energy measurements for comparison in the plot. It can be seen that the new results are in good agreement with the lower energies. Only at higher transverse momentum the new data deviates from the other energy measurements which can be explained by better calibration of the 8 TeV data. Then the meson yield is extracted by integrating the subtracted invariant-mass distribution in a mass range around the fitted meson mass M_{π^0} and subtracting from this the integral of the linear part of the fit to remove background photon pairs.
The integration range for the π^0 is $(M_{\pi^0} - 0.035\ \mathrm{GeV}/c\ ^2, M_{\pi^0} + 0.010\ \mathrm{GeV}/c\ ^2)$ which corresponds to $(-11\langle n\sigma_\pi \rangle, 3\langle n\sigma_\pi \rangle)$ around M_{π^0}. The asymmetric range is needed to incorporate the bremsstrahlung tail on the left side of the distribution. For the π^0 raw yield

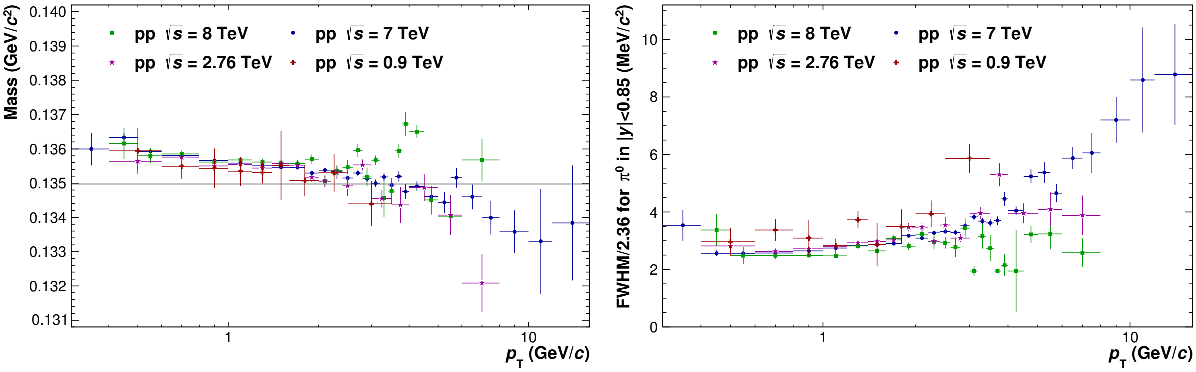

Figure 15: Mass of the neutral pion (**top**) and FWHM of the mass peak (**bottom**) depending on the p_{T} bin for the different energy measurements in pp collisions. The gray line indicates the nominal neutral pion mass of 0.135 GeV/c. Lower energy measurements from [3, 4].

the corresponding formula is given by:

$$N_{\mathrm{raw}}^{\pi^0} = \int_{M_{\pi^0}-0.035\mathrm{GeV/c^2}}^{M_{\pi^0}+0.010\mathrm{GeV/c^2}} (N^{\gamma\gamma} - N^{\mathrm{comb.BG}})\mathrm{d}M_{\gamma\gamma} - \int_{M_{\pi^0}-0.035\mathrm{GeV/c^2}}^{M_{\pi^0}+0.010\mathrm{GeV/c^2}} (B + C \cdot M_{\gamma\gamma})\mathrm{d}M_{\gamma\gamma} \quad (18)$$

In Figure 16 the resulting π^0 meson raw yield for pp collisions at different energies are shown. The spectra are normalized by the number of events N_{norm} given in Table 3 and by the bin width in p_{T}. The transverse momentum reach is limited by the statistics in the high p_{T} region and by background at low p_{T}. The measurements from the lower center of mass energies were done with the V0OR minimum bias trigger while the 8 TeV data was triggered with the V0AND minimum bias trigger.

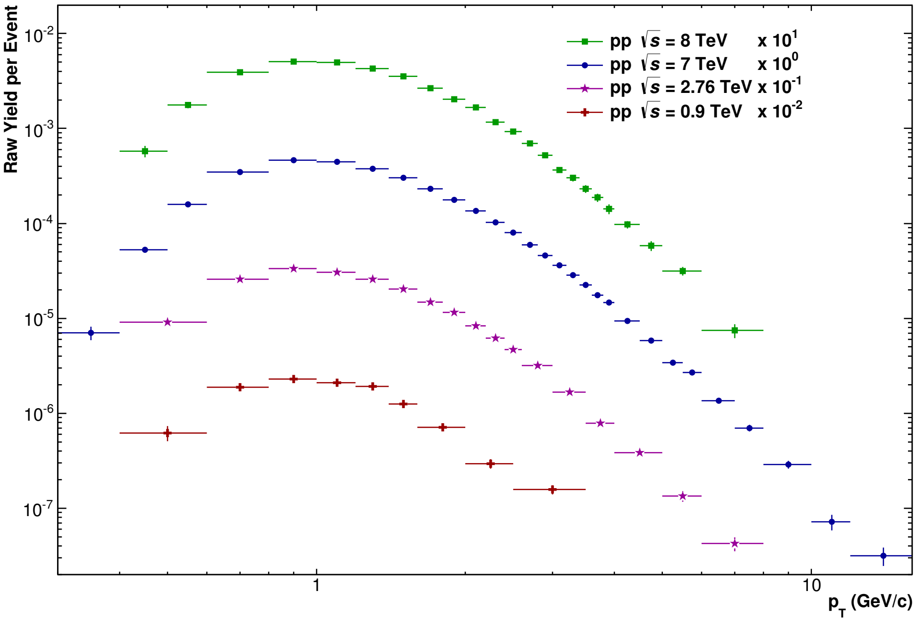

Figure 16: Raw yield of the π^0 meson in pp collisions at different energies as a function of the transverse momentum. The yield is normalized to the number of events N_{evt} and the spectra are divided by the bin width in p_{T}. Lower energy measurements from [3, 4].

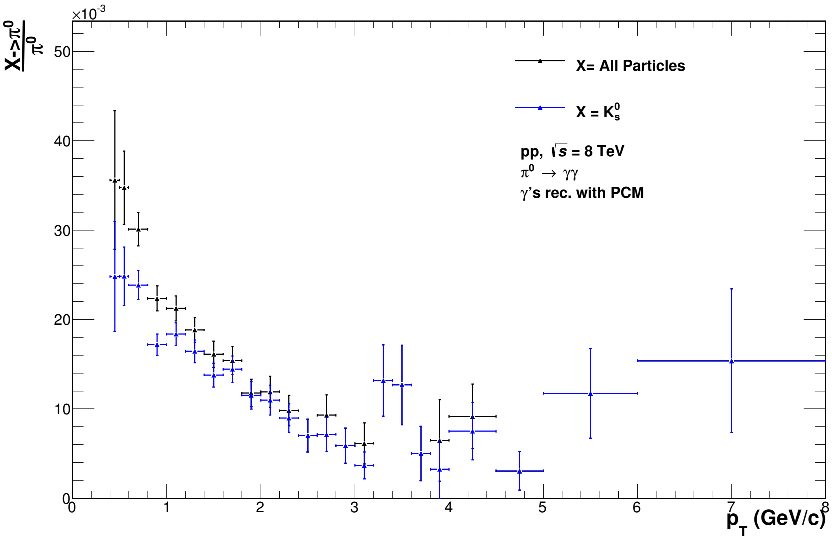

Figure 17: Ratio of reconstructed secondary π^0 mesons from K^0_s mesons (blue) or all secondary π^0 mesons (black) to the number of reconstructed neutral pions.

3.1.2 Pion Spectrum Corrections

Certain corrections to the raw yield of the mesons have to be applied. Secondary π^0 mesons originating from weak decays or hadronic interactions in the detector material need to be removed from the raw yield. Furthermore the contribution from out-of-bunch pileup π^0 mesons reconstructed in the TPC is an important factor to be considered. Then, geometrical acceptance and reconstruction efficiency are calculated from MC and corrected for. At last the spectra will be corrected for the finite bin width in p_{T}.

3.1.2.1 Correction for Secondary Neutral Pions

The contribution of secondary π^0 mesons from weak decays or hadronic interactions is removed by using the Monte Carlo simulations. The largest source of these mesons is the decay $K^0_s \rightarrow \pi^0\pi^0$ with a branching ratio of 30.7 %. In Figure 17 the fraction of secondary neutral pions to the total number of reconstructed pions can be seen for the 8 TeV data. The correction itself is done by multiplying the p_{T} dependent fraction of secondaries (black in Figure 17) with the measured raw yield and then subtract this value from the raw yields. In the future it might be necessary to adjust this contribution, due to a mismatch of the K^0_s spectra in data and MC as seen at lower center of mass energies.

3.1.2.2 Correction for Acceptance and Efficiency

With the raw yields corrected for secondary π^0 mesons the next step is to correct for the detector acceptance and efficiency. This is done by using the Monte Carlo simulations which provide additional information about particles that are created during the collision. The geometrical acceptance A_{π^0} is a transverse momentum dependent property of the detector and is defined as the ratio of π^0 mesons within $|y| < 0.85$ ($N_{\pi^0,|y|<0.85}$) whose daugther particles are within an acceptance of $|\eta| < 0.9$ to the total number of π^0 mesons that are created in the same rapidity window.

$$A_{\pi^0} = \frac{N_{\pi^0,|y|<0.85} \text{ with daughter particles within } |\eta_\gamma| < 0.9}{N_{\pi^0,|y|<0.85}} \tag{19}$$

In Figure 18, the geometrical acceptance for π^0 mesons can be seen for different collision energy measurements. As for the analysis of the different energies the same y cut was used, the acceptance is the same for all within the errors.
The reconstruction efficiency is determined by applying the same analysis that was used on the real data to the simulated data but with the addition that each photon pair is verified to originate from the same π^0 with Monte Carlo information. This leads to a suppression of the combinatorial background. The reconstruction efficiency can be seen in Figure 18 for different energy measurements.

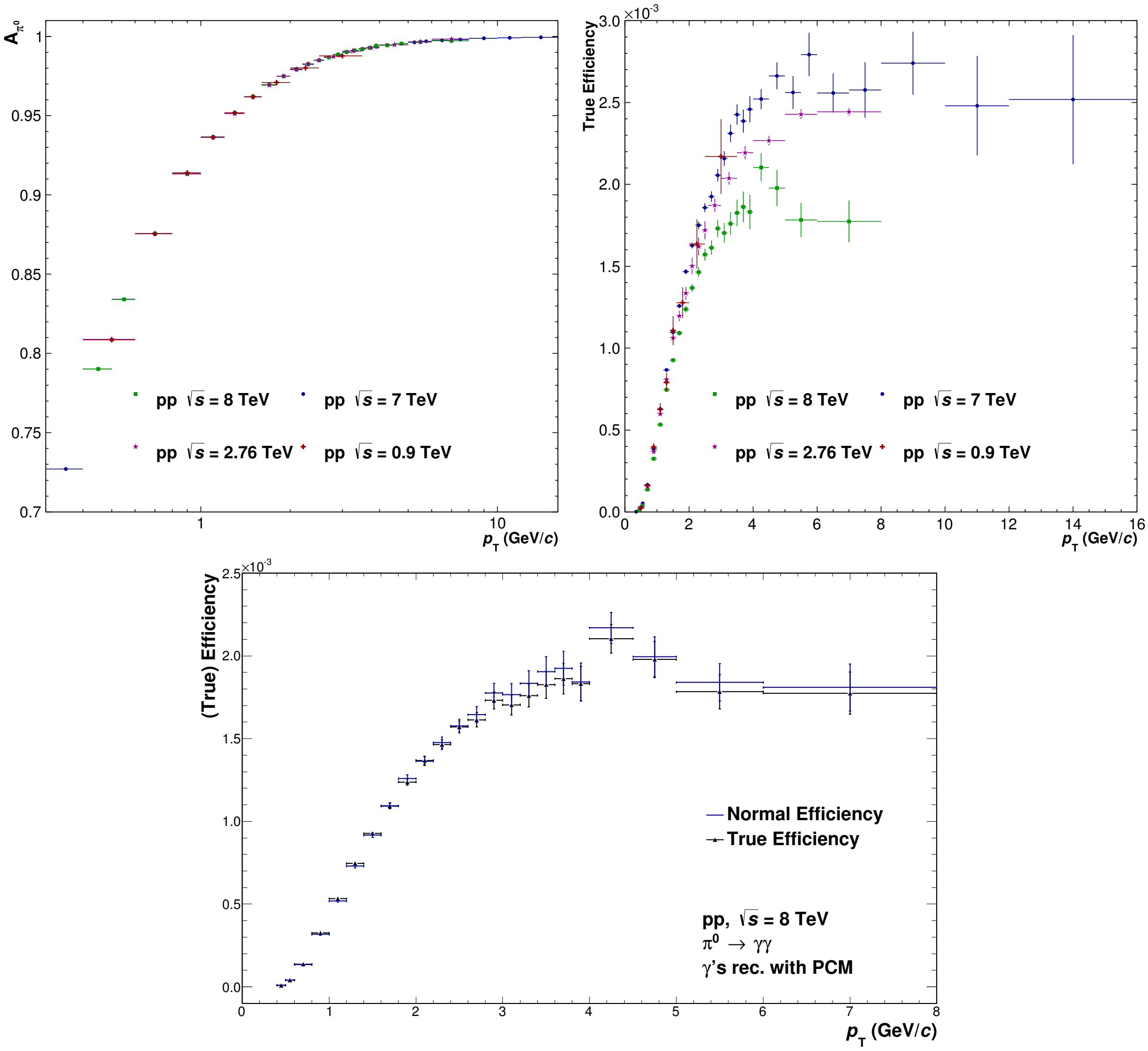

Figure 18: Left: Geometrical acceptance and **Right:** the reconstruction efficiency for π^0 mesons in pp collisions for different collision energies. Lower energy measurements from [3, 4]. **Bottom:** True efficiency and normal efficiency for $\sqrt{s} = 8$ TeV.

The p_{T} dependent conversion probability and the photon reconstruction efficiency determine the shape of the reconstruction efficiency as both photons and their conversion products need to be in the acceptance of the detector and they have to reach the TPC to be reconstructed. This leads to a slow rise of the efficiency until it levels out at about 4 GeV/c transverse momentum. The conversion probability ($\approx$ 8.6%) and the reconstruction efficiency itself $\approx$ 68% enter quadratically in the meson reconstruction efficiency and this leads to a maximum efficiency of about 0.34 % for the mesons. Due to the tight photon cuts for the analysis this value cannot be reached by the simulation. The cuts for this analysis are also tighter than for the lower energy measurements which leads to a lower efficiency for 8 TeV compared to the other energy measurements as seen in Figure 18.
An additional validation of the true efficiency is made by applying the same method as is the signal extraction and then comparing the efficiency from this method to the true efficiency. As expected both efficiency are consistent within the uncertainties as seen in Figure 18. This also cross checks the quality of the background extraction from 3.1.1 which therefore does not produce an additional systematic error source.

3.1.2.3 Correction for Finite Bin Width

Due to different widths in the transverse momentum binning of the π^0 meson spectra which increases for higher p_{T} a correction for the true bin value is needed. As the underlying spectrum is steeply falling, the yield in one of those p_{T} bins is not the yield at the bin center, instead the data points have to be shifted horizontally to represent the real transverse momentum at the bin center. In this analysis of pp collisions the spectra are shifted by assuming a Tsallis function [54] as an approximation of the underlying spectrum.

$$E\frac{\mathrm{d}^3N}{\mathrm{d}p^3} = \frac{1}{2\pi p_{\mathrm{T}}}\frac{\mathrm{d}^3N}{\mathrm{d}y\mathrm{d}p_{\mathrm{T}}} = \frac{1}{2\pi}\frac{\mathrm{d}N}{\mathrm{d}y}\frac{(n-1)(n-2)}{nT^{\mathrm{eff}}(nT^{\mathrm{eff}}+m(n-2))}\left(1+\frac{\sqrt{p_{\mathrm{T}}^2+m^2}-m}{nT^{\mathrm{eff}}}\right)^{-n} \tag{20}$$

In this function the parameters m and $\sqrt{m^2+p_{\mathrm{T}}^2} = m_{\mathrm{T}}$ represent the meson mass and the transverse mass, while the parameters $\frac{\mathrm{d}N}{\mathrm{d}y}$, T^{eff} and n are determined via the fit. The influence of this correction strongly depends on the bin width and the steepness of the underlying spectrum. As seen in Figure 19 the correction ranges from about 1-4% below 5 GeV/c up to 15% at higher p_{T} depending on the bin width.

3.1.2.4 Correction for Neutral Mesons from Out of Bunch Pileup Vertices

Since 2010 the luminosity has been continuously increased and the filling scheme has been changed drastically from single bunches in the beginning of 2010 to trains of bunches in the end of 2010. The main filling scheme for 2012 and the 2012 peak luminosity can be seen in Figure 20. This scheme consists of 1380 bunches with a spacing of 50ns. The problem with this many bunches and their small spacing in the LHC is that the algorithms used in ALICE are not designed to reconstruct more than one primary vertex at a time. In addition the drift velocity of the charges in the TPC, which is about 2.7cm/μs, produce a readout time of about 92 μs (the same time a bunch needs for a full revolution in the LHC). The long readout time leads to an overlap of the events in the TPC as the information of every event happening within one LHC revolution is stored inside the TPC

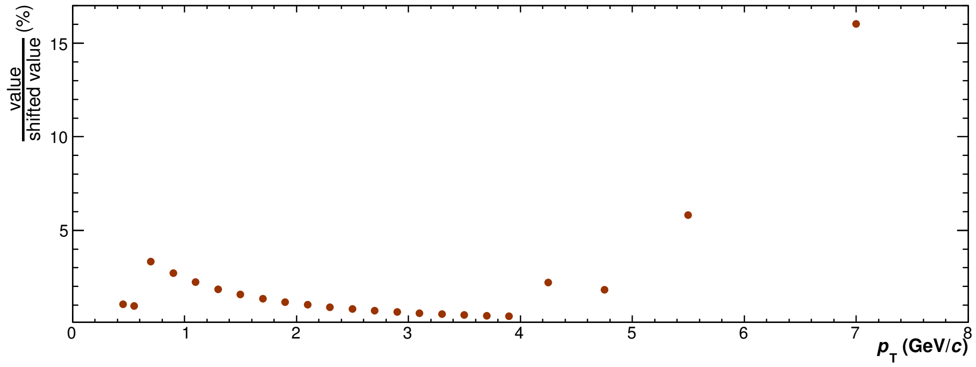

Figure 19: Ratio in percent between the spectra before and after correction for the finite bin width.

drift chamber. This overlap and the fact that the reconstruction algorithm in the TPC only focuses on resolving one primary vertex at a time requires an out of bunch pileup rejection.

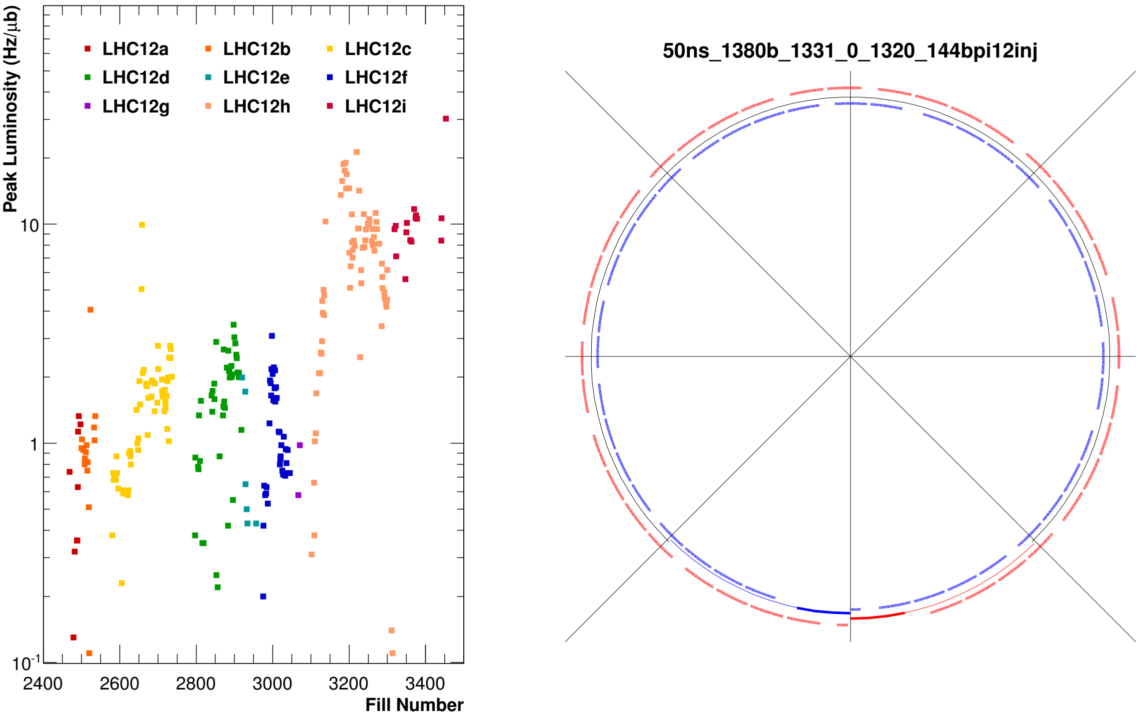

Figure 20: Peak luminosity of the LHC in 2012 [39] for the ALICE experiment (**left**) and predominant LHC filling scheme [38] for the period LHC12c (**right**).

To correct for this, the distance of closest approach (DCA) is used. It is represented by a distance called dca_z in the beam direction (z) and is the smallest distance to the straight line going from the primary vertex to the conversion point in direction of the momentum vector. The dca_z distribution for photons in LHC12[a-d] can be seen in Figure 34.

It is possible to reconstruct three different types of photons with the conversion method which then are put into different categories:

1. both legs are TPC only tracks (case for all photons with $R_{\mathrm{conv}} \geq 50$ cm)
2. one of the electrons has at least 2 ITS hits
3. both legs have at least 2 ITS hits

Category 1 contributes about 45% of the final yield in LHC12[a-d], while category 2 makes up 15% and category 3 about 27%. In general category 2 should contribute very little as it is unlikely to have one leg with more than 2 ITS clusters, while the other leg doesn't have a hit. Dead areas in the ITS lead to an increased number in category 2. Also it can be possible that both electrons pass too closely to each other through the same sensor and cannot be resolved as two separate clusters.

For mesons however there are six different categories which are momentum dependent:

1. both photons from category 1
2. one photon from category 1 and one photon from category 2
3. one photon from category 1 and one photon from category 3
4. both photons from category 2
5. one photon from category 2 and one photon from category 3
6. both photons from category 3

Figure 21 (top left) shows, for the periods LHC12[a-d] of the 8 TeV data, the fraction of neutral pions for the different categories relative to all neutral pions for each momentum bin. Category 1 shows the largest contribution especially at low p_{T} and in comparison, category 2 and 3 are more suppressed as they are required to come from the primary vertex. For the category 6 where both photons are constrained to the primary vertex there will be no pileup contribution, however this condition only holds for a small fraction of the photons.

For an estimation of the background there are three different methods to which correspond different functions.

Method A For this method a function called 'ShowBackground' is used which is implemented in TH1. For the 8 TeV data 12 iterations and a background smoothing of 5 was used.

Method B It uses a Gaussian distribution for the dca_z distribution with a hole around zero to exclude the peak but it requires rather high statistics for a good fit.

Method D The last method is like Method A but with a slightly higher smoothing applied.

In Figure 34 (Top) the fit of Method A to the dca_z distributions (blue line) can be seen while in Figure 34 (Bottom) the fit of the different methods for category 1 can be seen. Then the different methods are analyzed and multiplied by the fraction of mesons in the respective category. Figure 21 (top right) shows the fraction of background due to pileup

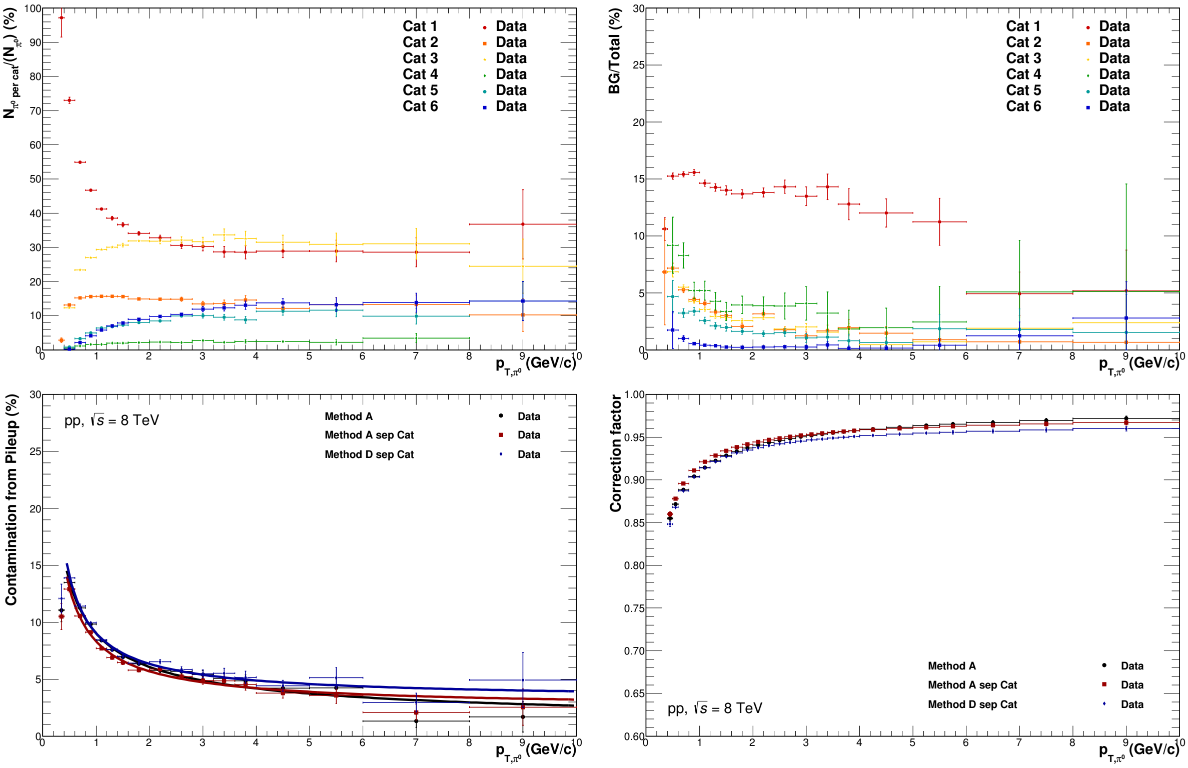

Figure 21: Top left: Fraction of the neutral pions in the respective categories for pp at $\sqrt{s} = 8$ TeV with respect to the total amount of neutral pions measured in the data sample. **Top right:** Fraction of the neutral pions originating in pileup vertices with respect to the inclusive measured neutral mesons in the respective category. **Bottom left:** Contamination from pileup to the inclusive neutral pion yield. **Bottom right:** Final correction factor due to neutral pions originating from pileup vertices. Data from LHC12[a-d].

for the different categories. Here only category 1 to category 3 are important as the other categories have a rather low impact on the data.

With the pileup studies, the influence on the neutral pion yield can be calculated and is shown in Figure 21 (bottom left) for the different methods used for fitting the dca_z distribution. As expected, the low p_{T} region in comparison to the high p_{T} region shows a huge pileup contribution as it is dominated by the TPC photons. From the contamination from pileup vertices the correction factor due to pileup can be calculated and is shown in Figure 21 (bottom right). At low p_{T} this factor ranges from 15-10% and levels out at high transverse momentum to about 5%.

3.1.3 Systematic Error Evaluation

The cuts for the selection of tracks, electrons, photons and mesons are varied in order to estimate the systematic error for the π^0 meson. The variation of these cuts either samples the underlying Gaussian distribution (i.e. variation of the pion rejection cut) or determines the maximum deviation (i.e. variation of the single track momentum cut). The contribution of each cut variation is determined by only varying one cut at a time and then the differences in the fully corrected spectra are calculated.

$$\Delta(p_{\mathrm{T}}) = \left(\frac{\mathrm{d}^2 N}{\mathrm{d}y\mathrm{d}p_{\mathrm{T}}}\right)_{\mathrm{modified}}(p_{\mathrm{T}}) - \left(\frac{\mathrm{d}^2 N}{\mathrm{d}y\mathrm{d}p_{\mathrm{T}}}\right)_{\mathrm{standard}}(p_{\mathrm{T}}) \tag{21}$$

$$\sigma_{\Delta}(p_{\mathrm{T}}) = \sqrt{\left|\sigma^2_{\left(\frac{\mathrm{d}^2 N}{\mathrm{d}y\mathrm{d}p_{\mathrm{T}}}\right)_{\mathrm{modified}}}(p_{\mathrm{T}}) - \sigma^2_{\left(\frac{\mathrm{d}^2 N}{\mathrm{d}y\mathrm{d}p_{\mathrm{T}}}\right)_{\mathrm{standard}}}(p_{\mathrm{T}})\right|} \tag{22}$$

The calculation of the systematic errors within one cut is done on a bin by bin basis. In each bin the average of the maximum deviation in both directions from the standard cut is taken as the systematic error for the particular cut variation. In Table 8 the detailed variations except the yield extraction can be found for the pp $\sqrt{s} = 8$ TeV systematic error evaluation. There are five main categories for the systematic error sources:

Material Budget

The largest contribution to the total systematic error with 9.00% is the systematic error on the material budget. The detailed calculations can be found in [16] where differences between the two V^0 finders and also different Monte Carlo generators were used. As this systematic error is based on the R distribution of the photon candidates there is no additional variation of the R cut in the error evaluation.

Signal Extraction

In this category the cut variations for the energy asymmetry α of the two photons and the actual signal extraction error are considered. The latter is estimated by a variation of the integration windows for the signal extraction and also the normalization range of the background. In Table 7 these variations can be seen. The signal extraction error contributes to the total systematic error by a large amount (2-8%). The systematic error due to the energy asymmetry was smoothed as the error showed unphysical fluctuations which overestimated the contribution to the systematic error due to a lack of statistic.

Integration range	
standard	$(M_{\pi^0} - 0.035,\ M_{\pi^0} + 0.010)$ GeV/c^2
narrow	$(M_{\pi^0} - 0.015,\ M_{\pi^0} + 0.005)$ GeV/c^2
wide	$(M_{\pi^0} - 0.055,\ M_{\pi^0} + 0.025)$ GeV/c^2

Table 7: Variations of the integration windows for the systematic error estimation from the signal extraction.

Track Reconstruction

The contributions to this category are all related to the secondary track sample. It includes the TPC cluster over findable cluster cut and the minimum transverse momentum cut. At low p_{T}, this category dominates the systematic error while at higher transverse momenta it only contributes with 1% to the total systematic error. The single p_{T} systematic error was also smoothed above 1 GeV/c as in this transverse momentum region the contribution from this cut variation should be very low as it has a negligible impact on the yield there.

Quantity	Standard	Cut Variation1	Cut Variation2	Cut Variation3
dE/dx e-line				
$\sigma_{\mathrm{d}E/\mathrm{d}x,e}$	$-3 < \sigma < 5$	$-4 < \sigma < 5$	$-2.5 < \sigma < 4$	
dE/dx π-line				
π rej. low p				
$\sigma_{\mathrm{d}E/\mathrm{d}x,\pi}$	< 2	< 1	< 2.5	< 3
$p_{\text{min, }\pi\text{ rej.}}$	0.4 GeV/c	0.3 GeV/c	0.5 GeV/c	
single p_{T} $e^{\pm}$	> 0.05 GeV/c	> 0.075 GeV/c	> 0.1 GeV/c	
χ^2 γ	< 30	< 50	< 20	< 15
min TPC clust./ find. clust.	> 0.6	> 0.7	> 0.35	
$q_{\mathbf{T,max}}$	< 0.05 GeV/c	< 0.03 GeV/c	< 0.07 GeV/c	
α **meson**	< 0.8	< 0.75	< 0.85	
cos(P.A.)	< 0.85	< 0.9	< -1	
Ψ_{pair}	< 0.1	< 0.05	< 0.2	< 0.035

Table 8: Variations for the systematic error evaluation in pp collisions at $\sqrt{s} = 8$ TeV. The "Standard" column stands for the standard cut while the "Cut variation" columns show the variations that are applied to the standard cut. Only one cut (row) is changed at a time to estimate the systematic error.

Electron PID

In this category all cuts concerning the electron identification or pion rejection are considered which includes all the σ cuts on the TPC dE/dx. The contribution from this category to the total systematic error is p_{T} dependent and accounts for 1-7% of the error.

Photon Reconstruction

The systematic error from the cut on q_{T} as well as the two dimensional cut on χ^2 and Ψ_{Pair} contribute to this category. The contribution from the 2D cut in χ^2 and Ψ_{Pair} was set to a smoothed parabola to reduce statistical and unphysical fluctuations. Both values were smoothed with the same function as they are strongly correlated. The q_{T} cut was smoothed with a similar function but with a lower starting value and a stronger rise to account for the larger contribution at high transverse momentum. This category adds up to 2-9% of the total systematic error and is strongly p_{T} dependent.

In Figure 22 the final systematic errors for the $\sqrt{s} = 8$ TeV pp collisions for the π^0 are visualized. The detailed tables can be found in the Appendix in Table 15. The systematic error is dominated by the material budget error which was determined [16] to be 9% over the whole p_{T} range for pp collisions. The total systematic error range is 9-15% in the p_{T} region where the signal extraction is stable and enough statistic is available.

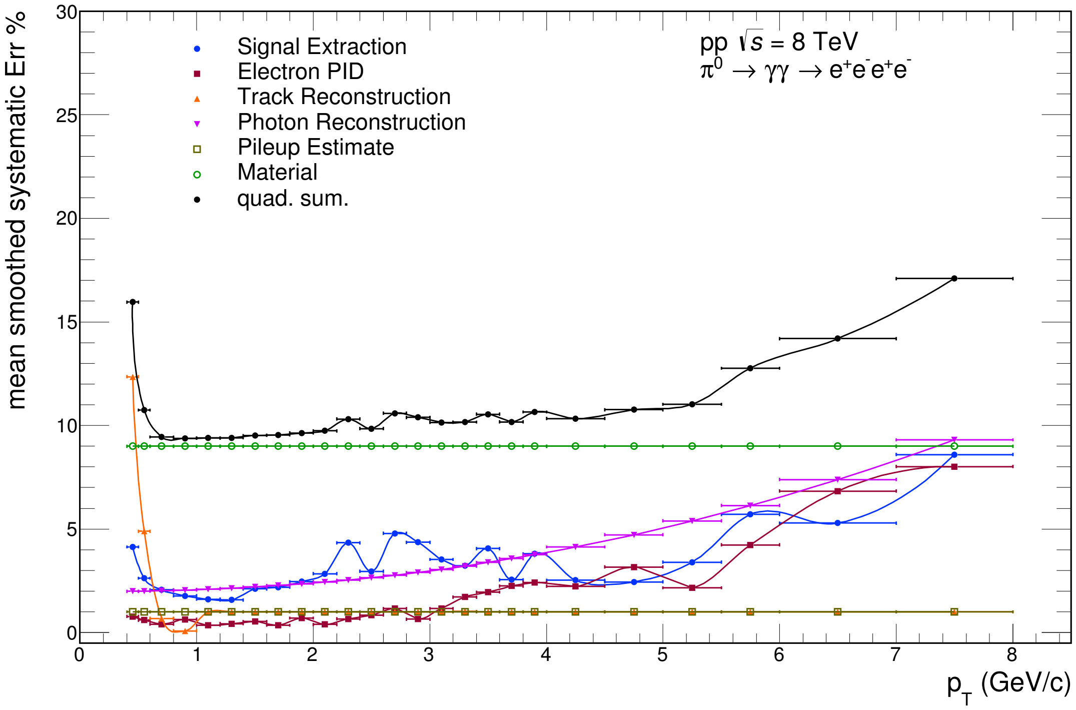

Figure 22: Visualization of the systematic errors for pp collisions at $\sqrt{s} = 8$ TeV. Indicated with colored points are the individual error sources. The final systematic error for the π^0 is represented with the black points.

3.2 Corrected Spectra

3.2.1 Invariant π^0 Meson Yield

Taking all corrections from the previous section into account, the fully corrected invariant π^0 meson yield can be calculated using

$$E\frac{\mathrm{d}^3N}{\mathrm{d}p^3} = \frac{\mathrm{d}^3N}{p_\mathrm{T}\mathrm{d}p_\mathrm{T}\mathrm{d}y\mathrm{d}\phi} = \frac{1}{2\pi}\frac{1}{p_\mathrm{T}}\frac{\mathrm{d}^2N}{\mathrm{d}y\mathrm{d}p_\mathrm{T}} = \frac{1}{2\pi}\frac{1}{N_\mathrm{evt.}}\frac{1}{p_\mathrm{T}}\frac{1}{\epsilon_{\mathrm{reco},\ \pi^0}}\frac{1}{A_{\pi^0}}\frac{1}{\mathrm{BR}}\frac{N^{\pi^0}}{\Delta y\Delta p_\mathrm{T}}. \tag{23}$$

Here $N_\mathrm{evt.}$ is the number of events as seen in Table 3. The branching ratio of the decay $\pi^0 \to \gamma\gamma$ is represented by BR and N^{π^0} is the number of reconstructed π^0 mesons within the rapidity range $[-0.8, 0.8]$ and the transverse momentum bin Δp_T. p_T stands for the corrected transverse momentum of the bin after the correction for the finite bin width Δp_T. ϵ_reco is the reconstruction efficiency and A_{π^0} is the acceptance as shown in Figure 18.

The fully corrected invariant yield for $\pi^0 \to \gamma\gamma$ can be seen in Figure 23 for the 8 TeV minimum bias data as well as for lower center of mass energy measurements including statistical and systematical errors. The data from the lower center of mass energy measurements was taken with the V0OR minimum bias trigger while the 8 TeV data was taken with the V0AND MB trigger. The difference between both triggers is a factor of $\mathrm{MB}_\mathrm{AND}/\mathrm{MB}_\mathrm{OR} \approx 0.87$ at 7 TeV for the trigger efficiencies.

The π^0 meson could be reconstructed with the PCM in a transverse momentum range from 0.4 to 8 GeV/c with systematic errors of the order of 9.5-11% at mid p_T. This

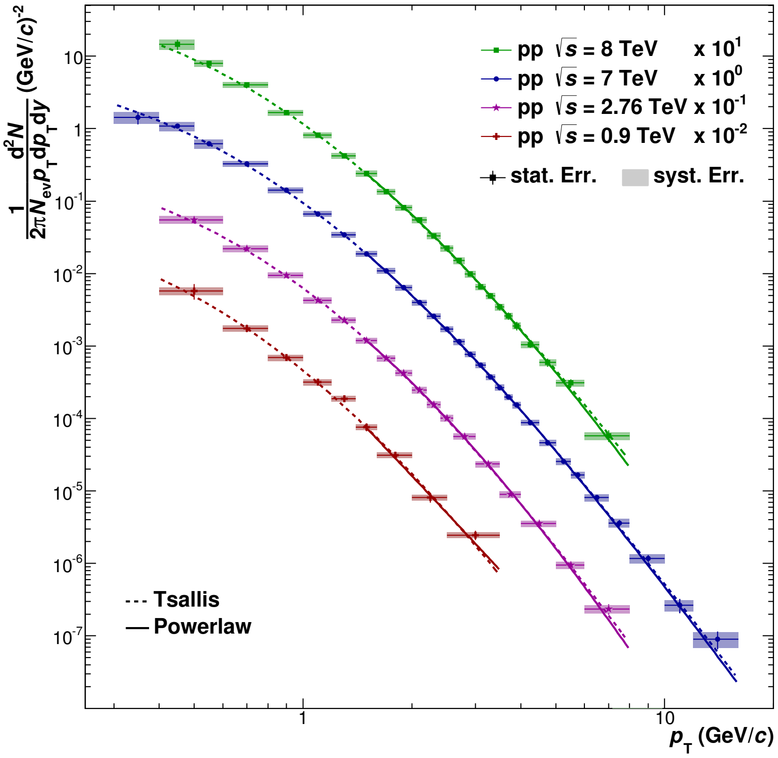

Figure 23: Fully corrected invariant yield of the π^0 meson in pp collisions at different energies as a function of the transverse momentum. The yield is normalized to the number of events N_{evt} and the spectra are divided by the bin width in p_{T}. The data is from PCM only. The shaded boxes represent the systematical error while the lines stand for the statistical error. Lower energy measurements from [3, 4].

systematic error is comparable to the systematic errors estimated in the 7TeV, 2.76 TeV and 900 GeV measurements. Even though the spectrum is not as smooth as the 7 TeV spectrum it still follows the same trend. In addition it is in agreement with the Tsallis and Powerlaw fits that represent several models depending on the transverse momentum region. This can be seen in Figure 23 where the agreement with the fits is given within the uncertainties. Here the powerlaw fit is the most common fit used to describe the p_{T} dependence of the spectrum at high momentum. It is in good agreement with the data above a transverse momentum of 1.5 GeV/c. The fit function for the powerlaw is given by

$$E\frac{\mathrm{d}^3N}{\mathrm{d}p^3} = A_{\mathrm{pow}} \cdot \frac{2(n_{\mathrm{pow}}-1)(n_{\mathrm{pow}}-2)}{\pi}\frac{(n_{\mathrm{pow}}-3)^2}{p_{\mathrm{T}}}\left(\frac{1+2p_{\mathrm{T}}}{\langle p_{\mathrm{T}}\rangle(n_{\mathrm{pow}}-3)}\right)^{-n_{\mathrm{pow}}} \tag{24}$$

with n_{pow} being the power and A_{pow} as well as $\langle p_{\mathrm{T}}\rangle$ constant scaling factors. The results of the Tsallis and Powerlaw fits are displayed in Table 9. The powerlaw parameters for the 900 GeV yield are not included as there are only three data points for fitting and therefore the parameters are not well constrained.

	Tsallis-Fit			Powerlaw-Fit		
$\sqrt{s}$ (TeV)	$\frac{\mathrm{d}N}{\mathrm{d}y}$	T^{eff} (MeV/c^2)	n	A_{pow}	n_{pow}	$\langle p_{\mathrm{T}} \rangle$
8	3.41 ± 0.17	147 ± 5	6.93 ± 0.17	2.37 ± 0.62	6.84 ± 0.58	0.86 ± 0.06
7	2.40 ± 0.15	139 ± 4	6.88 ± 0.07	2.64 ± 0.32	6.16 ± 0.15	0.79 ± 0.02
2.76	2.18 ± 0.24	126 ± 7	7.01 ± 0.17	1.39 ± 0.36	7.58 ± 0.62	0.82 ± 0.05
0.9	1.5 ± 0.3	132 ± 15	7.8 ± 0.5			

Table 9: Parameters of the Tsallis and Powerlaw fit to the corrected invariant yield in Figure 23. Parameters for the Tsallis fit of 0.9 TeV and 7 TeV from [3] and for 2.76 TeV from [4].

3.2.2 π^0 Meson Cross Section

The fully corrected differential invariant cross section can be calculated using

$$E\frac{\mathrm{d}^3\sigma}{\mathrm{d}p^3} = \frac{1}{2\pi}\frac{1}{p_{\mathrm{T}}}\frac{\sigma_{\mathrm{MB_{V0AND}}}}{N_{\mathrm{evt.}}}\frac{1}{\epsilon_{\mathrm{reco},\,\pi^0}}\frac{1}{A_{\pi^0}}\frac{1}{\mathrm{BR}}\frac{N^{\pi^0}}{\Delta y \Delta p_{\mathrm{T}}}. \tag{25}$$

Here the variables are the same as for the corrected yield calculation but with $\sigma_{\mathrm{MB_{V0AND}}} = (55.74 \pm 0.46)$ μb [10] being the cross section for the V0AND minimum bias trigger. The differential invariant cross section therefore is the corrected yield scaled by $\sigma_{\mathrm{MB_{V0AND}}}$ and can be seen in Figure 24. The fits from the corrected yield can therefore be also scaled and applied to the π^0 meson cross section. In addition the ratio between data and fits is plotted in the same figure for the different energy measurements. This ratio shows the good agreement between data and fit as it is consistent with unity over a large transverse momentum range.

From Table 9 the evolution of the fit parameters with increasing center of mass energy can be seen. For the 8 TeV data the parameter $\frac{\mathrm{d}N}{\mathrm{d}y}$ is higher compared to the lower energies while n and T^{eff} are comparable to 7 TeV and 2.76 TeV. The parameter $\frac{\mathrm{d}N}{\mathrm{d}y}$ stands for an estimate of the total yield at $y = 0$ and shows the expected increase of the total yield with increasing center of mass energy. The parameter n can be treated like the parameter n_{pow} from a power law function and therefore shows the steepness of the spectrum. Within the uncertainties it can be observed that n decreases with increasing center of mass energy what can be interpreted as a flattening of the spectra for higher $\sqrt{s}$. As shown in [16] the parameter T^{eff} is species dependent and within the uncertainties the 8 TeV fit parameter is consistent with those from lower energy measurements.
The powerlaw parameters show the same behaviour as those from the tsallis fit. A_{pow} is comparable to $\frac{\mathrm{d}N}{\mathrm{d}y}$ from the tsallis fit and also shows an increasing value with increasing center of mass energy. The power n_{pow} shows a decreasing value and therefore also a flattening of the spectrum for higher $\sqrt{s}$.

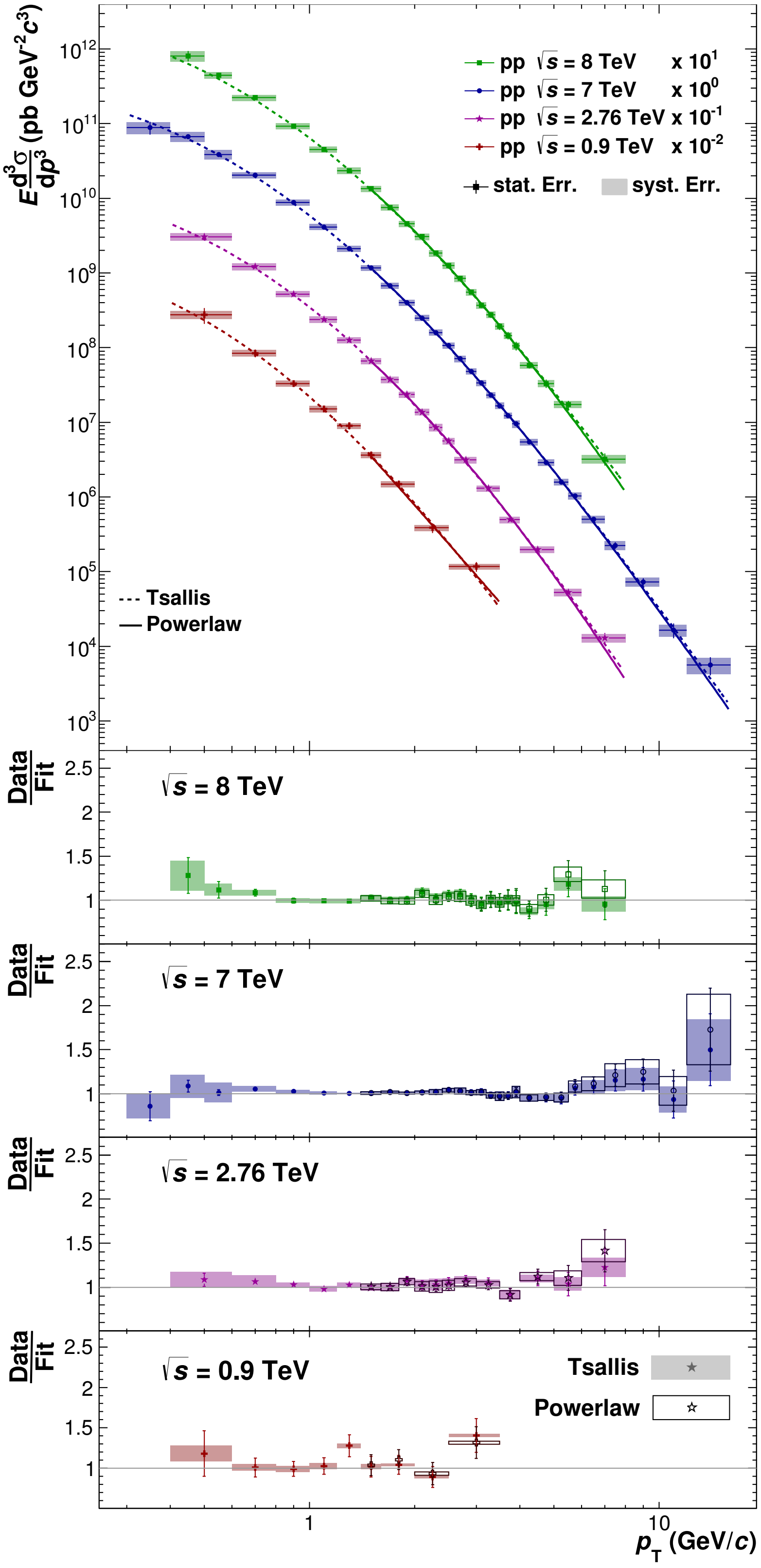

Figure 24: Top: Differential invariant cross section of the π^0 meson in pp collisions at different energies as a function of the transverse momentum. The data is from PCM only. **Bottom:** Ratio of the data and the fit functions of the π^0 meson differential invariant cross section in pp collisions at different energies. The boxes represent the systematical error while the lines stand for the statistical error. Lower energy measurements from [3, 4].

4 Trigger Analysis

In this section the influence of different level-0 (L0) and level-1 (L1) triggers on the photon and π^0 meson yield will be shown. An overview of the different detectors of the ALICE experiment is given in Table 2 where the detectors used as triggers in the analysis are marked with a star (*). In addition the number of events for each trigger used in this analysis is given in the appendix in Table 16.

4.1 EMCal Trigger

The EMCal was installed in 2010 to enhance the jet measuring capabilities of the ALICE detector and to provide an unbiased jet trigger. The EMCal allows to take data in three different trigger classes, one level 0 trigger and two L1 triggers, their purpose is described in Table 10. [5, 45]

trigger	function
L0 E0	enhances events with large energy deposit in the EMCAL
L1 EJE	enhances the probability of events with large jet contribution on the EMCAL surface
L1 EGA	enhances number of collected events with large photon/electron energy

Table 10: Different EMCal subtriggers and their function [5].

The EMCal L0 trigger E0 fires about 1.2 μs after the interaction if the energy summed over a sliding windows von 4x4 towers (2x2 FastOR) is higher then a threshold above the background noise. The 4x4 towers are required to be inside one Trigger Region Unit (TRU) which corresponds to 8x48 towers (4x24 FastOR). The combination of three nearby TRUs is called a supermodule and in 2012 there were 10.6 supermodules (32 TRUs) installed.

The EMCal L1 triggers fire about 6.2 μs after the interaction. The L1 photon trigger (EGA) compares the energy summed over a sliding window of 4x4 towers to a multiplicity dependent threshold from the V0. For this L1 trigger the 4x4 towers can also cross the border to another TRU unit which increases the effective surface by about one third. The jet trigger (EJE) sums the energy over a patch consisting of 3x3 subregions while one subregion is defined as 8x8 towers and compares it to a multiplicity corrected threshold.

Spectrum	$\frac{\mathrm{d}N}{\mathrm{d}y}$	T^{eff} (MeV/c^2)	n	χ^2/NDF
γ yield	$(7.53 \pm 1.41) \cdot 10^{6}$	615 ± 67	10.74 ± 1.14	1.33
π^0 yield	$(1.34 \pm 0.08) \cdot 10^{-2}$	432 ± 29	8.29 ± 0.64	0.98

Table 11: Parameters of the Tsallis fit to the kINT7 minimum bias raw yield from LHC12[a-i].

Figure 25 shows that the minimum bias data collected for photons and neutral pions does not provide enough statistics to produce the ratio with the triggered data above 15 GeV/c. They are therefore fitted with a Tsallis function to reach higher p_{T} and the parameters of the Tsallis fits can be seen in Table 11. For the γ spectrum a fit range of 4.5-25 GeV/c

was chosen to reduce the influence from the uncorrected low p_{T} points. The π^0 spectrum was fitted above 1.8 GeV/c to exclude the falling spectrum at low transverse momentum.

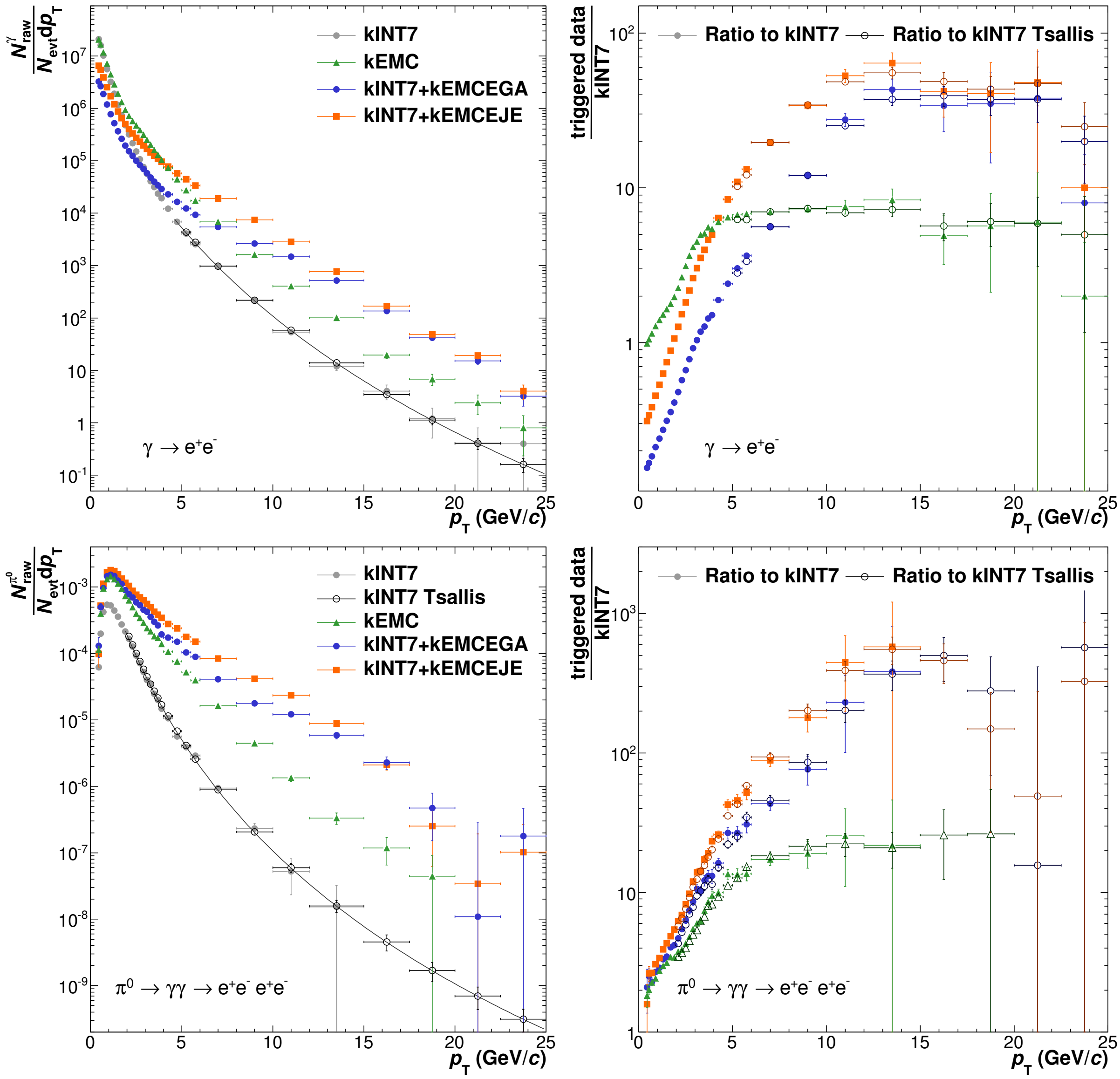

Figure 25: Raw photon (**top**) and π^0 yields (**bottom**) for the EMCal subtriggers and their ratios (**right**) with respect to the kINT7 minimum bias trigger. kEMC corresponds to the L0 EMCal trigger (E0) and kEMCEGA and kEMCEJE are the L1 triggers in coincidence with the minimum bias (kINT7) trigger. The data is merged from LHC12[a-i] to get high enough statistics.

The fits allow to produce the ratios seen in Figure 25 (right) also at higher p_{T}. Therefore the influence of the EMCal L0 and L1 triggers on the photon and π^0 meson raw yield can be compared to the minimum bias (kINT7) yield over a large transverse momentum range. The photon yield is increased by the L1 triggers above the threshold of 2 GeV/c [48] and rises by a factor of 500-1000 at higher transverse momentum. Due to the ad-

ditional surface the L1 triggers cover, the triggered data is much cleaner and therefore shows a higher yield compared to the L0 triggered data. The L0 trigger levels out after about 5 GeV/c at a factor of 8-10 compared to the minimum bias.
The same behavior can be observed for the π^0 yield where the L0 trigger also starts to saturate above 5 GeV/c while the L1 triggers produce cleaner triggered data.

4.2 TRD Trigger

The TRD trigger which was introduced in the 2012 pp runs is designed to allow to enhance the statistics at high transverse momentum for various particles. This is possible due to the different L1 subtriggers which all aim for high p_{T} particles. The TRD only receives a fraction (10-25 kHz) of the L0 MB events to evaluate them for a L1 decision. Therefore four algorithms were implemented: jet trigger (HJT), single electron trigger (HSE), quarkonium electron trigger (HQU) and TRD+EMCal electron trigger (HEE). An overview of these algorithms can be seen in Table 12 but the HEE algorithm is left out as it was not used during data taking. The jet trigger is used for different physics and shows its full potential only at very high transverse momenta ($>$ 100 GeV/c) and will therefore not be discussed in this analysis.

trigger	function
TRD HQU	quarkonia electron trigger (electron candidate with $p_{\mathrm{T}} > 2$ GeV/c)
TRD HSE	single electron trigger (electron candidate with $p_{\mathrm{T}} > 3$ GeV/c)
TRD HJT	jet trigger (3 tracks with $p_{\mathrm{T}} > 3$ GeV/c in one stack)

Table 12: Different TRD L1 triggers and their trigger conditions [5].

During data taking in 2012 there were 13 TRD supermodules installed with five stacks each. A stack in the TRD as required for HJT are 6 layers of chambers in radial direction which cover $\Delta\eta \approx \Delta\Phi \approx 0.1$ in pseudorapidity. The L1 triggers make their decision about 7.7μ after the interaction and can only be initiated by a L0 trigger [2]. The decision is based on chamber-wise track segments (tracklets) and the tracks which the Global Tracking Unit (GTU) reconstructs from them.

For the comparison between minimum bias (kINT7) and the triggered data the Tsallis fit from the last subsection with the parameters in Table 11 was used. In Figure 26 the photon and π^0 meson raw yield of the different TRD L1 triggers is plotted.
In the γ raw yield, the single electron trigger HSE and the quarkonia trigger HQU show distinct turn on curves around 3 and 2 GeV/c respectively. These kinks in the yield come from the trigger conditions which require an electron candidate with a transverse momentum above 3 or 2 GeV/c. In the π^0 spectrum this kink is slightly smeared out due to the fact that a π^0 meson requires four electrons for a reconstruction instead of two which are required for a single photon.
The yield increase for both L1 triggers is about a factor of 10-20 for the photon yield and a factor of 50-100 for the π^0 meson yield at high p_{T}. It is expected that the L1

triggers saturate at high transverse momentum. This behavior could not be observed as the uncertainties, due to the lack of statistics in the minimum bias and the errors from the minimum bias fit, are still too large.

This short trigger analysis has shown that with the L1 trigger algorithms the γ and π^0 meson raw yield at high p_{T} can be significantly improved.

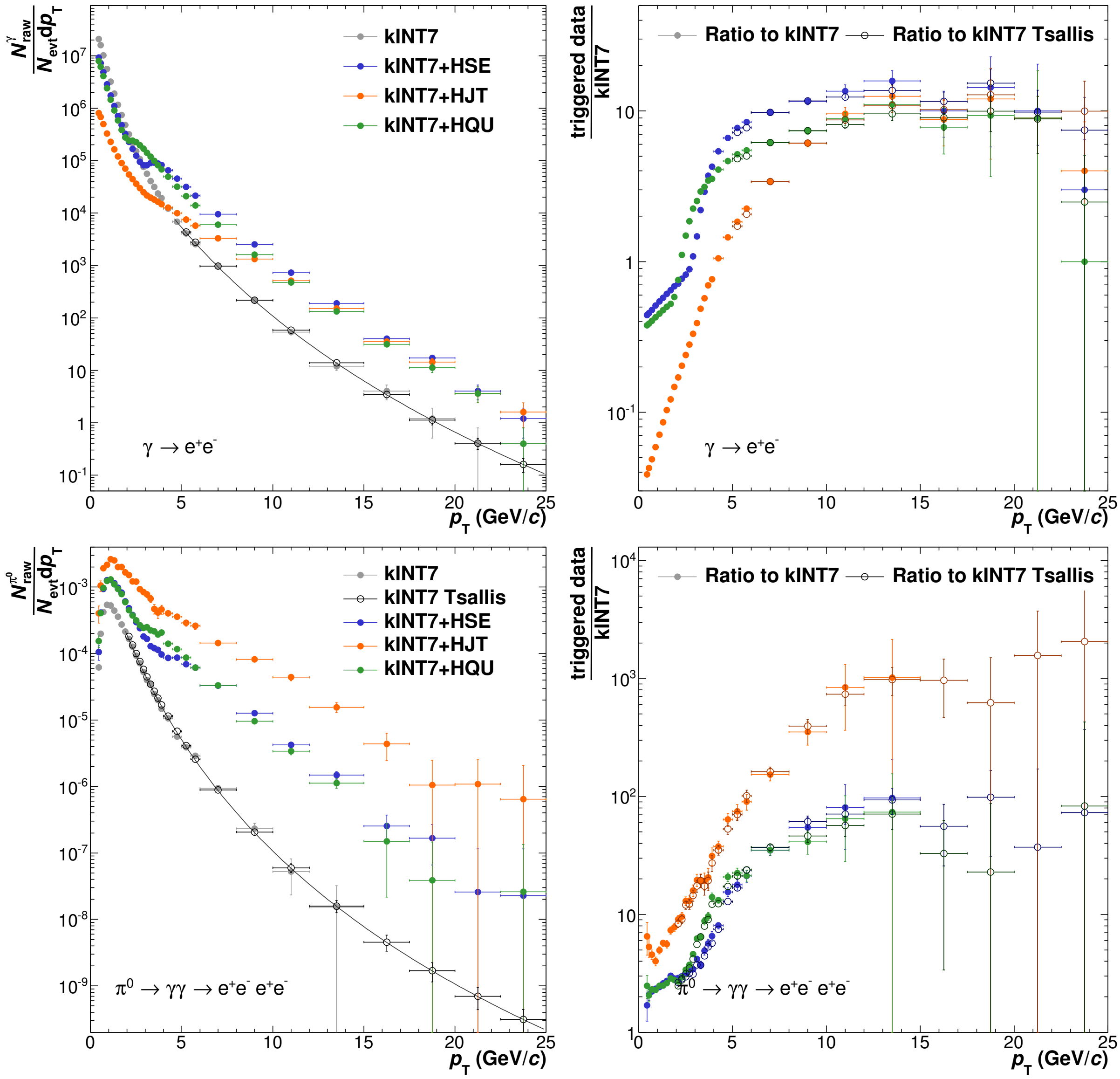

Figure 26: Raw photon (**top**) and π^0 yields (**bottom**) for the TRD L1 triggers and their ratios (**right**) with respect to the kINT7 minimum bias trigger. The single electron (HSE), the jet (HJT) and the quarkonia trigger (HQU) are the L1 triggers in coincidence with minimum bias (kINT7). The data is merged from LHC12[a-i] to get high enough statistics.

5 Summary and Outlook

In this thesis the neutral pion differential invariant yield and cross section in proton-proton collisions at $\sqrt{s} = 8$ TeV has been presented. The data used in this analysis was collected by ALICE in the data taking period in 2012 and corrected with PYTHIA8 and PHOJET Monte Carlo Simulations. Additionally the results were compared to lower center of mass energy measurements from data taking campaigns in 2010 and 2011.

For the extraction of the neutral pions the PCM method has been used. This method uses the reconstruction of the π^0 decay photons via electron and positron tracks using the Inner Tracking System and the Time Projection Chamber. The reconstructed photons are combined into pairs for which the invariant mass is calculated. The combination of every possible photon pair within one event produces a combinatorial background which is subtracted using the event mixing method. The strong π^0 peak in the remaining invariant mass spectrum is then fitted with a Gaussian distribution that is combined with an exponential tail to account for bremsstrahlung. The remaining combinatorial background is subtracted with a linear function that is included in the signal fit. The resolution of the π^0 mass peak (FWHM) has been shown to be similar to those from lower center of mass energy measurements with a resolution of 3-4 MeV/c^2. For the invariant yield of the π^0 an asymmetric integral around the peak has been used which incorporates the bremsstrahlung tail on the left side. The were then corrected using PYTHIA8 and PHOJET Monte Carlo Simulations.

As part of the quality assurance a method for the extraction of TPC photons and their decay products, which do not cross the border to another sector, has been developed. This method should provide direct information about the influences of voltage changes in the IROC and the OROC. In a further and closer analysis this method will be used on runs from LHC11h where such voltage changes were applied. There it will be checked if a change within the uncertainties can be observed.

Additionally the systematic errors for the 8 TeV dataset were estimated by investigating the influences of cut variations on the neutral pion yield. The cut variations account for contributions from the signal extraction, particle identification, photon reconstruction, tracking and pileup estimation. This lead to systematic errors of 9.5-11% in the region $0.6 < p_{\mathrm{T}} < 5.5$ GeV/c and up to 17% at 8 GeV/c. Therefore the systematic errors are comparable to those from the lower energy measurements.

Furthermore the shape of the spectrum has been compared to published results from lower center of mass energy measurements. This comparison has been made using two different fit functions: A Tsallis fit for the complete transverse momentum range and a Powerlaw fit for the high p_{T} region. From the fits a total yield increase and a clear flattening of the spectra at high p_{T} has been seen.
In order to enhance the statistics at high transverse momentum a trigger analysis has been performed which included triggers using the detector input from the TRD and EMCal. Both increased the photon and neutral pion yield significantly. The TRD trigger which was introduced in the data taking in 2012 showed distinct turn-on curves for its L1 single

and dielectron triggers. Those will be investigated further in the future as well as the EMCal photon trigger which also provides a strong enhancement at high p_{T}. Due to a lack of statistics, the minimum bias transverse momentum reach for the neutral pion has not been sufficient in order to be reliably compared to the triggered spectra above 15 GeV/c. Therefore its spectrum has been fitted above 1.8 GeV/c with a Tsallis function to reach higher p_{T}. This fit only serves as an approximation of the spectrum as the efficiency at high p_{T} is not known yet. Nonetheless within the uncertainties it has not been possible to make assumptions about trigger saturations as this would also require spectrum corrections especially for acceptance and efficiency. Therefore, the different triggers will be investigated in more detail in an upcoming analysis.

A Run Numbers for the Analysis

LHC12a 176701, 176704, 176730, 176749, 176752, 176753, 176854, 176859, 176924, 176926, 176927, 176929, 177157, 177160, 177167, 177173, 177180, 177182
LHC12b 177580, 177592, 177597, 177612, 177620, 177624, 177671, 177798, 177799, 177804, 177858, 177861, 177864, 177869, 177942
LHC12c 179618, 179621, 179639, 179802, 179803, 179858, 179859, 179917, 179918, 179920, 180000, 180042, 180044, 180127, 180129, 180130, 180131, 180133, 180199, 180200, 180500, 180501, 180515, 180561, 180564, 180567, 180569, 180719, 180720, 182017, 182018, 182022, 182106, 182110, 182111, 182207, 182289, 182295, 182297, 182299, 182300, 182302, 182322, 182323, 182325, 182624, 182684, 182687, 182692, 182728, 182729, 182730, 182740, 182741, 182744
LHC12d 184132, 184135, 184137, 184138, 184208, 184215, 184687, 184784, 184786, 185029, 185031, 185116, 185126, 185132, 185134, 185157, 185160, 185164, 185189, 185196, 185203, 185206, 185208, 185217, 185221, 185282, 185284, 185288, 185289, 185291, 185292, 185296, 185300, 185302, 185349, 185350, 185351, 185356, 185360, 185361, 185362, 185363, 185371, 185375, 185461, 185474, 185575, 185578, 185580, 185581, 185582, 185583, 185687, 185738, 185768, 185776, 185778, 185784, 186163, 186164, 186167, 186205
LHC12e 186602, 186601, 186598, 186514, 186511, 186508, 186507, 186460, 186459, 186453, 186429, 186428, 186389, 186388, 186387, 186386, 186385, 186365
LHC12f 188101, 188093, 187849, 187796, 187791, 187785, 187753, 187749, 187739, 187698, 187697, 187695, 187656, 187633, 187627, 187624, 187623, 187561, 187560, 187537, 187536, 187510, 187508, 187489, 187488, 187487, 187486, 187485, 187484, 187343, 187341, 187340, 187339, 187203, 187202, 187201, 187149, 187143, 187136, 187084, 187047, 186992, 186990, 186989, 186987, 186969, 186967, 186966, 186965, 186938, 186937, 186857, 186853, 186851, 186845, 186844, 186838, 186815, 186809, 186807, 186692, 186690, 186668
LHC12g 188503, 188500, 188499, 188490, 188455, 188454, 188449, 188448, 188447, 188446, 188444, 188443, 188442, 188440, 188366, 188365, 188364, 188363, 188362, 188359
LHC12h 189122, 189146, 189183, 189228, 189229, 189231, 189306, 189310, 189315, 189316, 189350, 189351, 189352, 189353, 189396, 189397, 189400, 189402, 189406, 189407, 189409, 189410, 189411, 189473, 189474, 189522, 189523, 189526, 189577, 189603, 189605, 189606, 189610, 189612, 189615, 189616, 189621, 189659, 189696, 189697, 189698, 189734, 189735, 189736, 189737, 190150, 190209, 190210, 190212, 190214, 190215, 190216, 190303, 190305, 190307, 190337, 190338, 190340, 190341, 190342, 190386, 190388, 190389, 190390, 190392, 190393, 190416, 190417, 190418, 190421, 190425, 190867, 190895, 190898, 190903, 190904, 190968, 190970, 190974, 190975, 190979, 190981, 190983, 190984, 191031, 191129, 191227, 191229, 191230, 191231, 191234, 191244, 191245, 191247, 191248, 191445, 191450, 191451, 192000, 192004, 192072, 192073, 192075, 192095, 192121, 192128, 192136, 192140, 192141, 192172, 192174, 192177, 192194, 192197, 192199, 192200, 192201, 192202, 192205, 192246, 192347, 192348, 192349, 192415, 192417, 192453, 192461, 192468, 192471, 192492, 192499, 192505, 192510, 192535, 192537, 192542, 192548, 192551, 192585, 192602, 192610, 192633, 192645, 192646, 192648, 192658, 192675, 192676, 192688, 192707, 192708, 192709, 192711, 192729, 192731, 192732

LHC12i
193701, 193698, 193693, 193194, 193193, 193192, 193189, 193188, 193187, 193156, 193155, 193153, 193151, 193148, 193097, 193094, 193093, 193092, 193051, 193049, 193047, 193014, 193011, 193010, 193008, 193007, 193005, 193004, 193000, 192824, 192822, 192820, 192779, 192778, 192775, 192772

Table 13: Runs used for the analysis.

B Additional Plots

B.1 Event Selection Plots

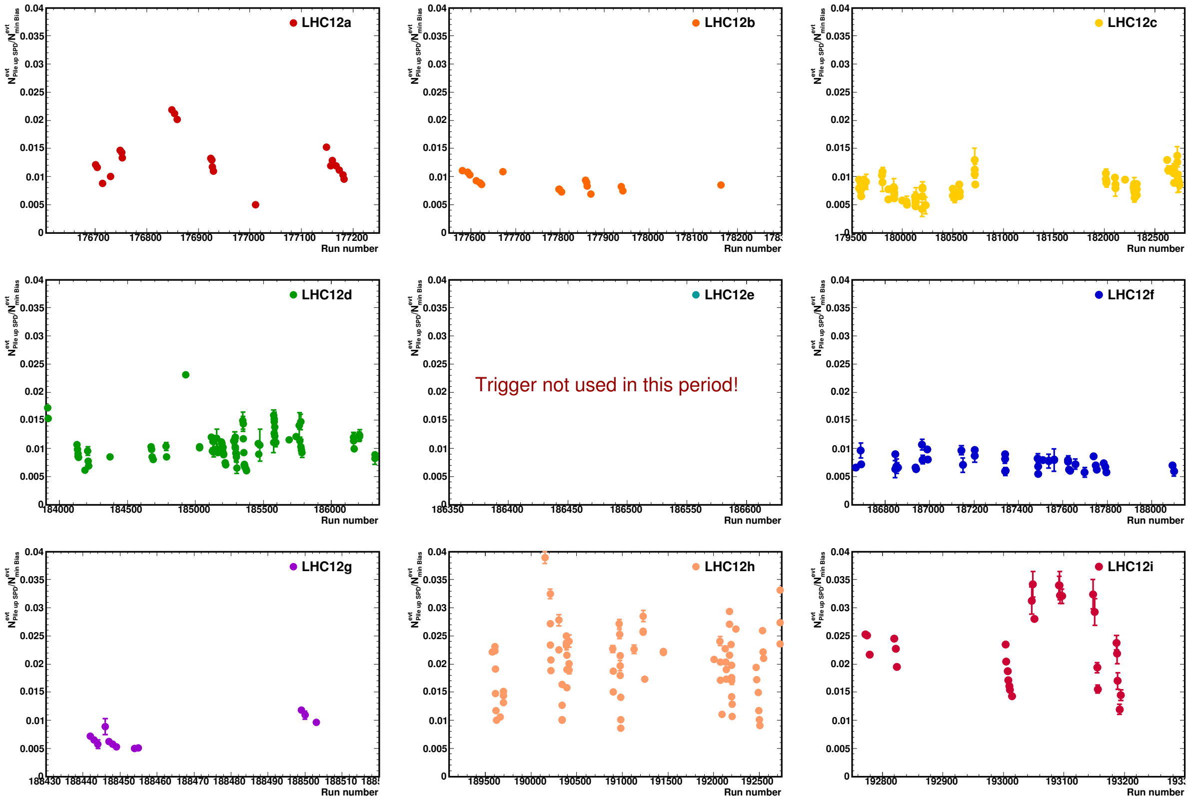

Figure 27: Fraction of events rejected due to the SPD Pileup condition with respect to the total number of collected minimum bias events in the respective run.

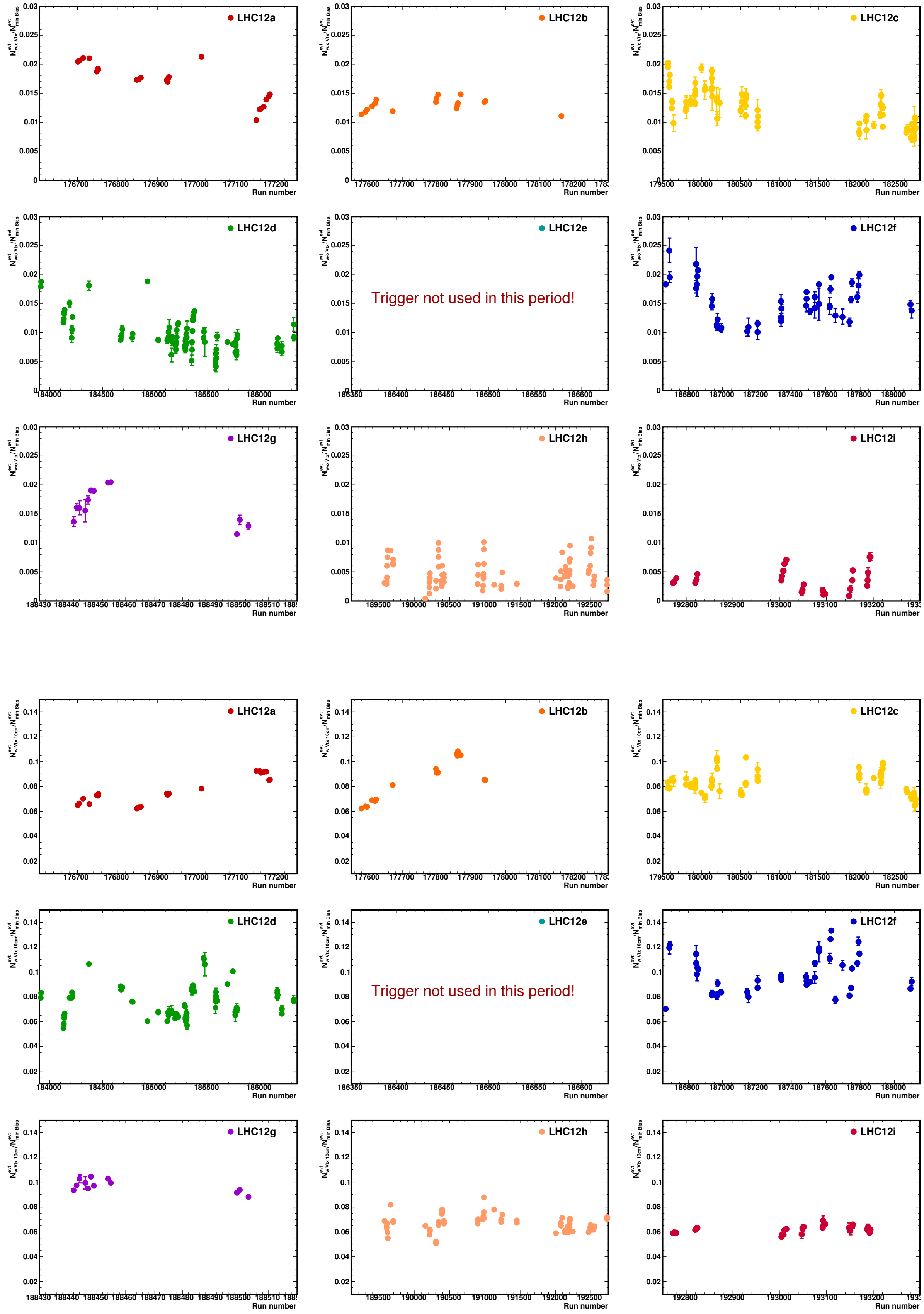

Figure 28: Fraction of events rejected due to missing primary vertex (**top**) and due to a vertex position outside $Z_{\mathrm{vtx}} = \pm 10$ cm (**bottom**) with respect to the total number of collected minimum bias events in the respective run.

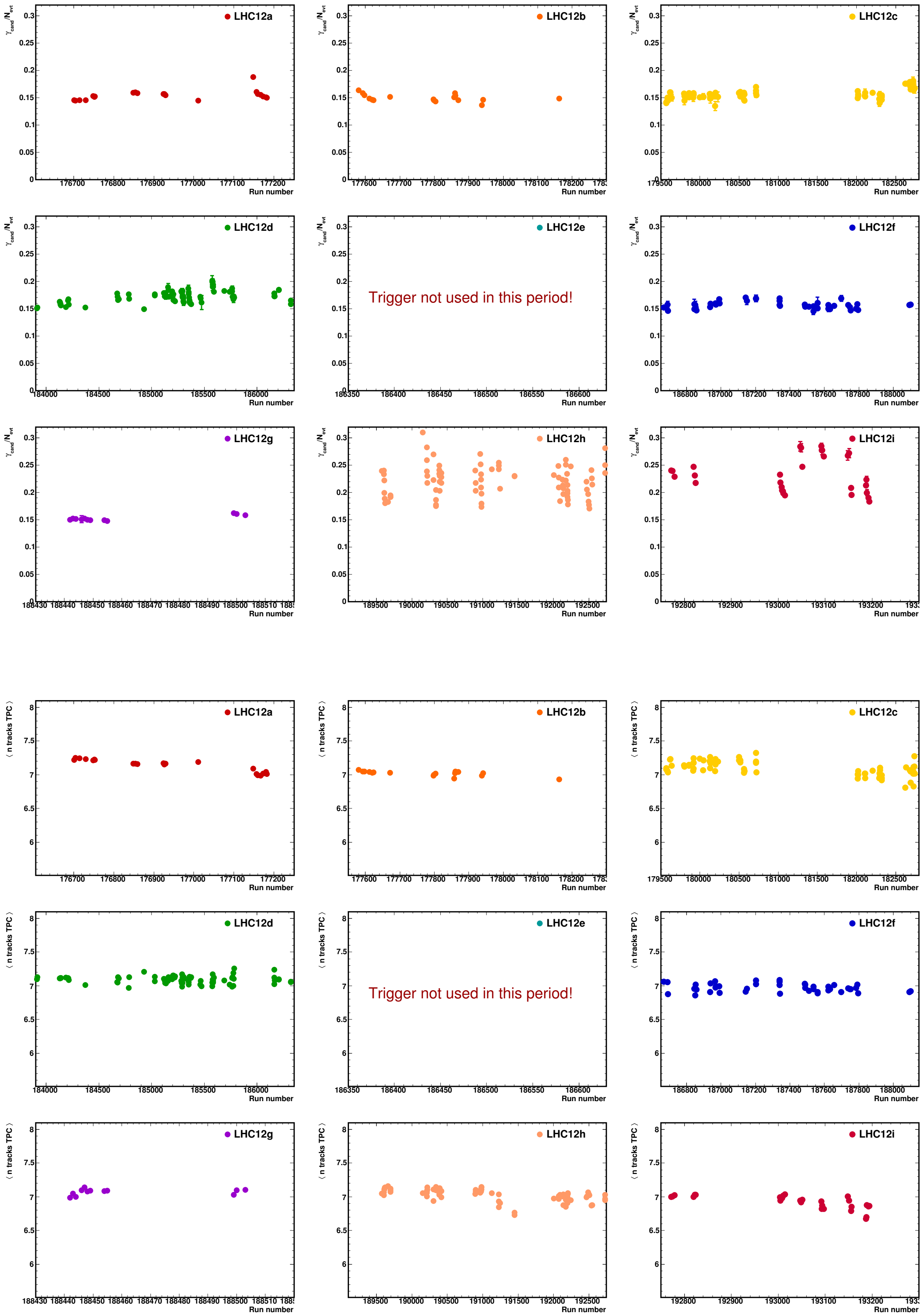

Figure 29: **Top:** Fraction of photon candidates normalized to the number of events, which fulfill the event selection criteria. **Bottom:** Mean number of primary tracks reaching the TPC versus run number for the periods LHC12a to LHC12i.

B.2 Data p_{T} Bins

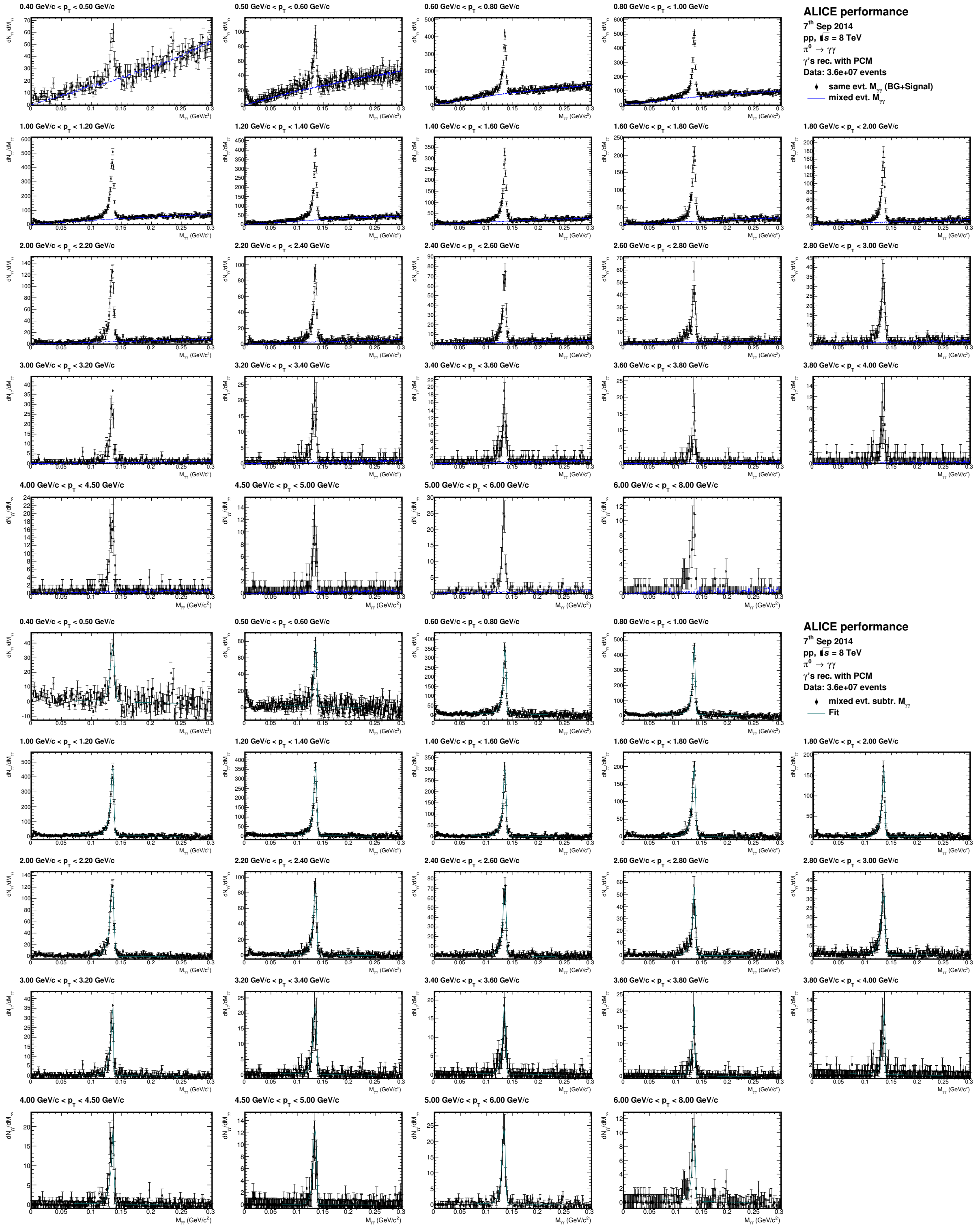

Figure 30: Invariant mass of the reconstructed photon pairs $M_{\gamma\gamma}$ in p_{T} bins from 0.4 to 10 GeV/c for the merged periods LHC12[a-d] minimum bias (kINT7) data before (**top**) and after (**bottom**) background subtraction.

B.3 Monte Carlo p_{T} Bins

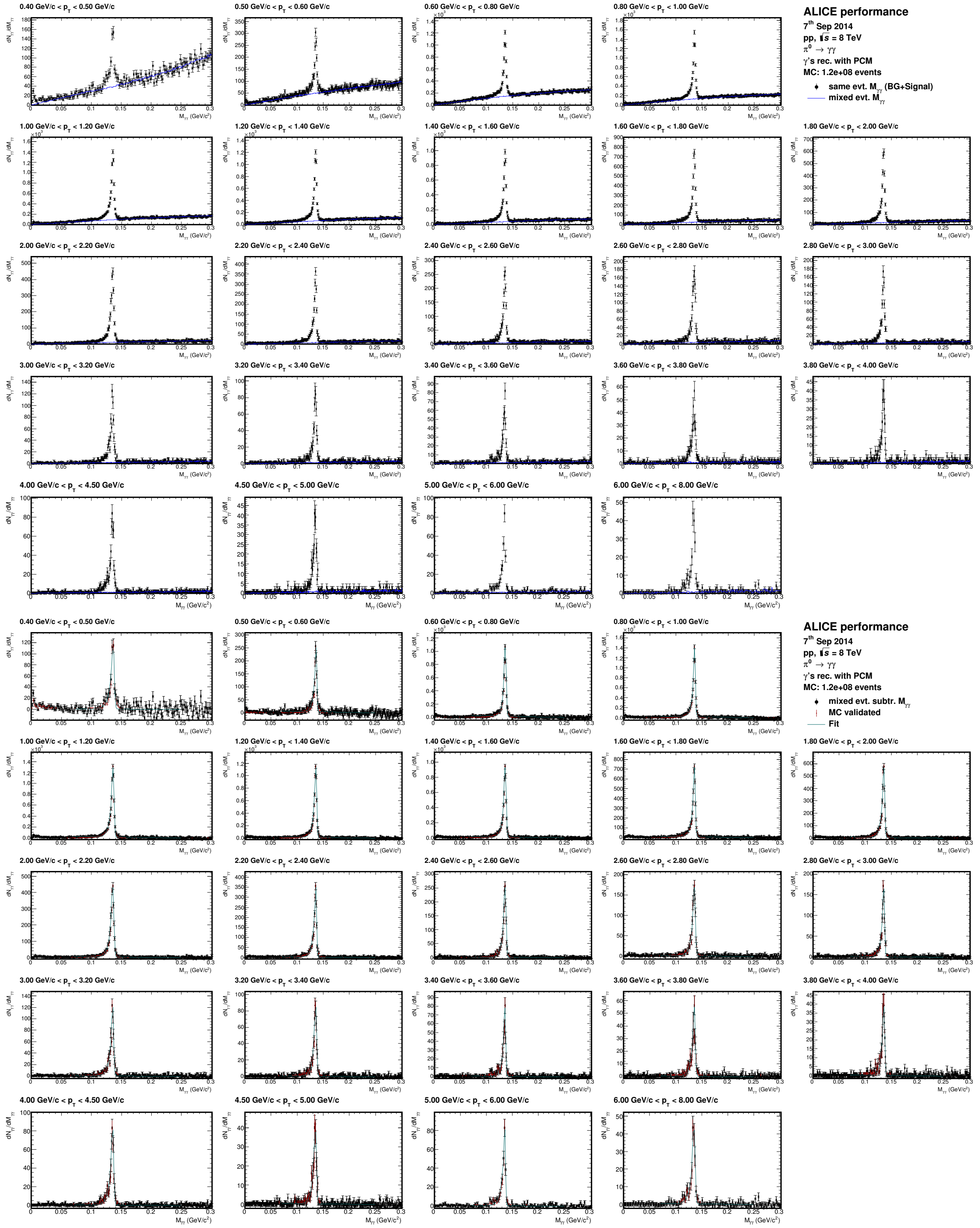

Figure 31: Invariant mass of the reconstructed photon pairs $M_{\gamma\gamma}$ in p_{T} bins from 0.4 to 10 GeV/c for the LHC12[a-d] minimum bias (kINT7) Monte Carlo data before (**top**) and after (**bottom**) background subtraction.

B.4 Detailed Systematic Errors

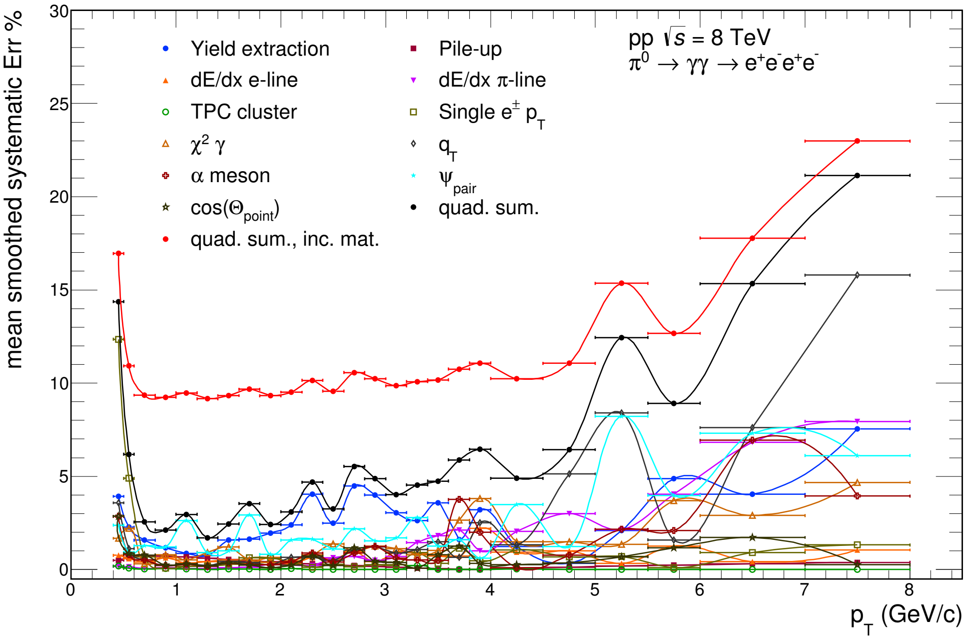

Figure 32: Visualization of the unsmoothed systematic errors for pp collisions at $\sqrt{s} = 8$ TeV. The individual error sources are indicated with the colored points. The total error for the π^0 meson spectra is represented by the red points.

p_{T} (GeV/c)	Material (%)	Yield Extr. (%)	PID e$^+$ e$^-$ (%)	γ rec. (%)	Track rec. (%)	Total (%)
0.45	9	4.59	0.78	4.61	12.35	16.95
0.55	9	2.46	0.60	2.64	4.89	10.90
0.7	9	2.03	0.41	1.41	0.69	9.33
0.9	9	1.68	0.64	1.46	0.08	9.22
1.1	9	2.76	0.35	2.69	0.16	9.45
1.3	9	1.17	0.43	1.30	0.19	9.14
1.5	9	1.86	0.53	1.63	0.28	9.31
1.7	9	3.35	0.35	2.99	0.63	9.66
1.9	9	2.12	0.70	0.93	0.61	9.31
2.1	9	2.87	0.39	1.77	0.41	9.51
2.3	9	4.36	0.67	1.93	0.12	10.1
2.5	9	2.72	0.84	1.82	0.28	9.57
2.7	9	4.99	1.16	2.62	0.14	10.56
2.9	9	4.29	0.65	2.33	0.26	10.23
3.1	9	3.49	1.17	2.22	0.26	9.86
3.3	9	3.83	1.71	3.09	0.94	10.08
3.5	9	3.79	1.95	2.21	0.34	10.17
3.7	9	2.26	2.24	3.16	1.14	10.75
3.9	9	3.26	2.42	4.60	0.46	11.07
4.25	9	3.71	2.24	4.03	1.04	10.25
4.75	9	1.27	3.17	5.48	0.67	11.06
5.25	9	8.49	2.16	11.83	0.70	15.36
5.75	9	6.30	4.23	5.66	0.10	12.67
6.5	9	8.35	6.83	10.95	0.92	17.77
7.5	9	9.71	8.01	17.57	1.32	22.98

Table 14: Detailed p_{T} dependent raw systematic error estimates for the different categories for π^0 meson measurements in pp collisions at $\sqrt{s} = 8$ TeV.

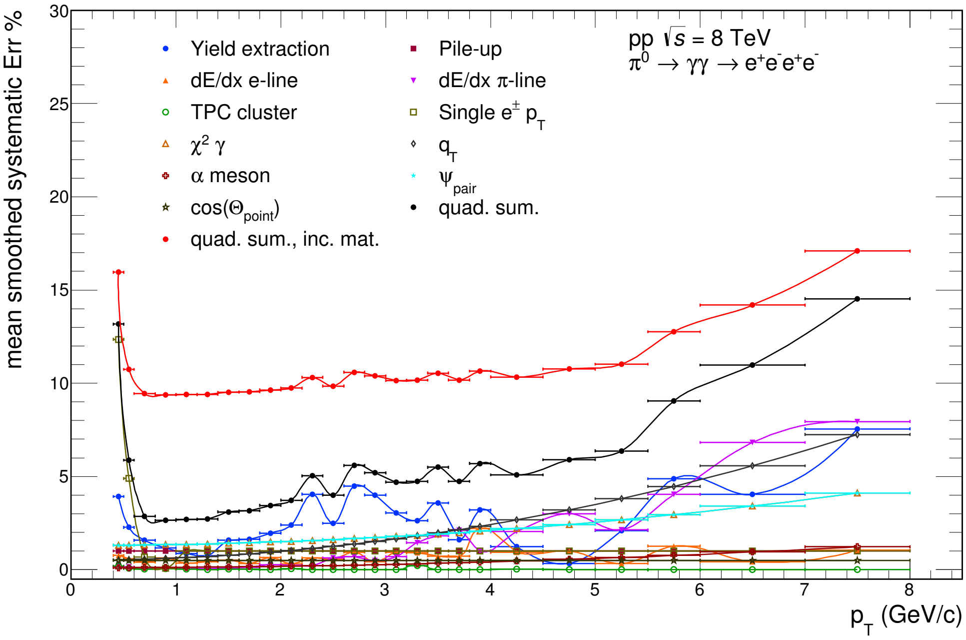

Figure 33: Visualization of the smoothed systematic errors for pp collisions at $\sqrt{s} = 8$ TeV. The individual error sources are indicated with the colored points. The total error for the π^0 meson spectra is represented by the red points.

p_T (GeV/c)	Material (%)	Yield Extr. (%)	PID e$^+$ e$^-$ (%)	γ rec. (%)	Track rec. (%)	Total (%)
0,45	9	4.14	0.78	1.99	12.35	15.96
0,55	9	2.63	0.60	2.00	4.89	10.75
0,7	9	2.06	0.41	2.02	0.69	9.45
0,9	9	1.78	0.64	2.05	0.08	9.38
1,1	9	1.61	0.35	2.09	1.00	9.39
1,3	9	1.57	0.43	2.14	1.00	9.40
1,5	9	2.11	0.53	2.20	1.00	9.52
1,7	9	2.18	0.35	2.27	1.00	9.54
1,9	9	2.46	0.70	2.35	1.00	9.64
2,1	9	2.84	0.39	2.44	1.00	9.74
2,3	9	4.34	0.67	2.54	1.00	10.31
2,5	9	2.96	0.84	2.65	1.00	9.85
2,7	9	4.79	1.16	2.77	1.00	10.59
2,9	9	4.35	0.65	2.91	1.00	10.39
3,1	9	3.53	1.17	3.05	1.00	10.15
3,3	9	3.22	1.71	3.21	1.02	10.17
3,5	9	4.05	1.95	3.38	1.00	10.54
3,7	9	2.55	2.24	3.57	1.00	10.17
3,9	9	3.81	2.42	3.76	1.00	10.65
4,25	9	2.53	2.24	4.13	1.00	10.34
4,75	9	2.45	3.17	4.73	1.00	10.76
5,25	9	3.40	2.16	5.39	1.00	11.03
5,75	9	5.70	4.23	6.14	1.00	12.77
6,5	9	5.29	6.84	7.39	1.00	14.20
7,5	9	8.60	8.01	9.31	1.00	17.10

Table 15: Detailed p_T dependent smoothed systematic error estimates for the different categories for π^0 meson measurements in pp collisions at $\sqrt{s} = 8$ TeV.

B.5 Trigger Analysis Dataset

Trigger in LHC12[a-i] **Min. Bias.**	Triggered Events N_{trig}	$\frac{\text{N+Vtx+}\lvert z_{vtx}\rvert\text{<10}}{\text{N}}$	$\frac{\text{N+Vtx+}\lvert z_{vtx}\rvert\text{>10}}{\text{N}}$	$\frac{\text{N+ no Vtx}}{\text{N}}$	$\frac{\text{N+Pile-up}}{\text{N}}$
kINT7	1.87e08	0.893	0.081	0.016	0.010
TRD triggered					
kINT7+HSE	2.14e07	0.903	0.059	0.001	0.038
kINT7+HJE	1.42e06	0.900	0.058	0.000	0.042
kINT7+HQU	1.84e07	0.902	0.059	0.001	0.039
EMCal triggered					
kEMC	3.85e07	0.909	0.067	0.001	0.024
kINT7+EGA	5.88e06	0.914	0.057	0.001	0.029
kINT7+EJE	1.04e07	0.908	0.057	0.001	0.034

Table 16: Number of events N and the fractions for $\frac{\text{N+Vtx+}\lvert z_{vtx}\rvert\text{<10}}{\text{N}}$, $\frac{\text{N+Vtx+}\lvert z_{vtx}\rvert\text{>10}}{\text{N}}$, $\frac{\text{N+ no Vtx}}{\text{N}}$ and $\frac{\text{N+Pile-up}}{\text{N}}$ for each trigger in the trigger analysis.

B.6 DCA p_{T} Bins

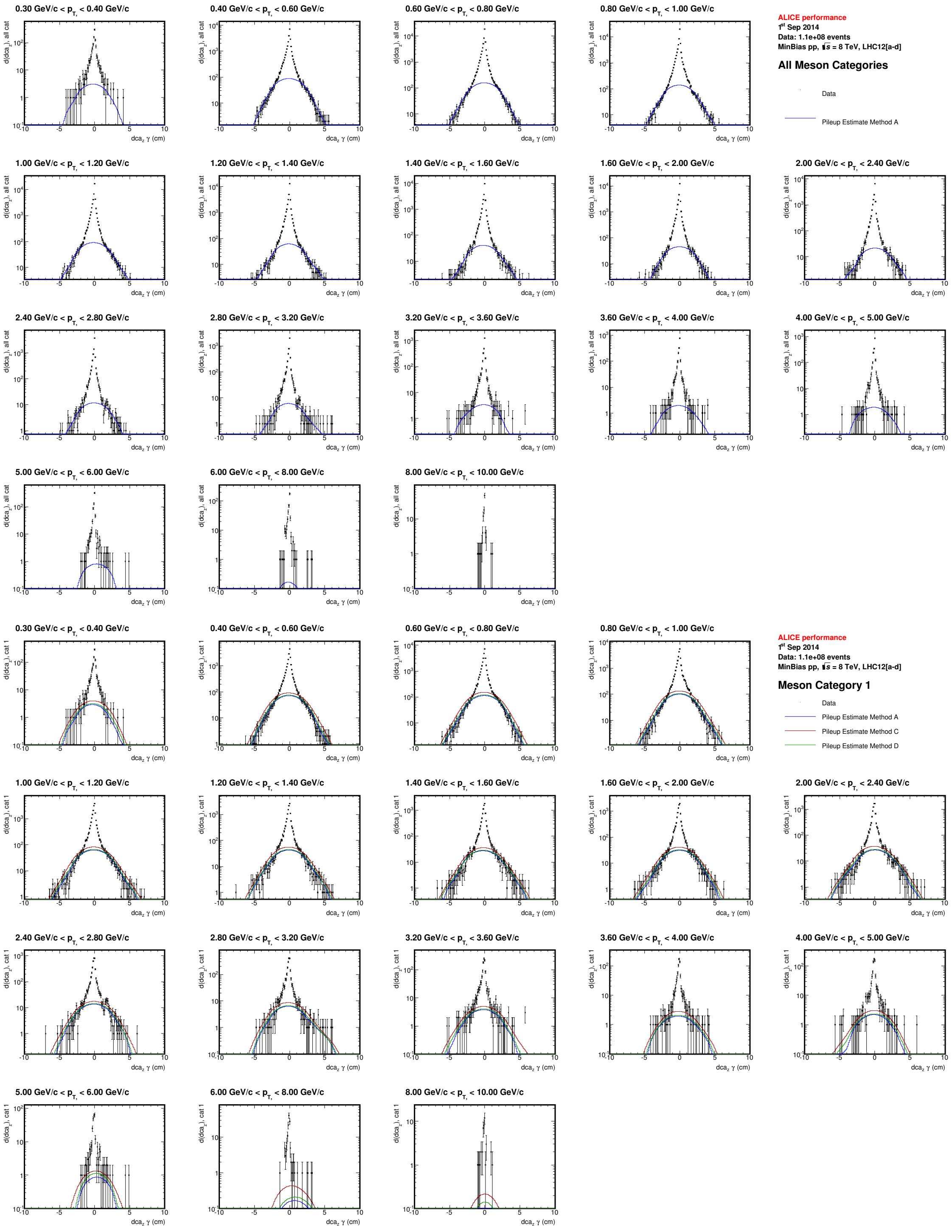

Figure 34: Top: dca_z distribution of photons from LHC12[a-d] for which the photon pair is in the invariant mass windows of 0.12 GeV/c $< M_{\gamma\gamma} <$ 0.145 GeV/c in different transverse momentum bins. The black points represent the measured data, while the blue line shows the background estimate via method A. **Bottom:** dca_z distribution of category 1 photons from LHC12[a-d] with background estimation methods A, C and D.

C Acronyms and Technical Terms

AGS	Alternating Gradient Synchrotron
ALICE	A Large Ion Collider Experiment
ATLAS	A Toroidal LHC Apparatus
BR	branching ratio
CERN	European Organization for Nuclear Research
CMS	Compact Muon Solenoid experiment
CTP	Central Trigger Processor
CP	charge parity
DAQ	Data Acquisition
DCA	distance of closest approach
DPM	Dual Parton Model
EMCal	Electromagnetic Calorimeter
HEE	TRD+EMCal electron trigger
FWHM	full width at half maximum
GTU	Global Tracking Unit
HMPID	High Momentum Particle Identification Detector
IROC	Inner Readout Chamber
ITS	Inner Tracking System
L0	level-0
L1	level-1
LEP	Large Electron Positron Collider
LHC	Large Hadron Collider
LHCb	LHC beauty experiment
LINACS	Linear Accelerators
LO	Leading Order
LQCD	Lattice QCD
MB	Minimum Bias

MC	Monte Carlo
MRPC	Multigap Resistive Plate Chamber
MTR	Muon Trigger
NLO	Next-to-Leading Order
OROC	Outer Readout Chamber
PHOS	Photon Spectrometer
PCM	Photon Conversion Method
PID	particle identification
pQCD	perturbative QCD
PS	Proton Synchrotron
PSB	Proton Synchrotron Booster
QA	Quality Assurance
QCD	Quantum Chromodynamics
QED	Quantum Electrodynamics
QGP	Quark-Gluon Plasma
RHIC	Relativistic Heavy Ion Collider
SDD	Silicon Drift Detector
SPD	Silicon Pixel Detector
SPS	Super Proton Synchrotron
SSD	Silicon Strip Detector
HJT	jet trigger
HSE	single electron trigger
HQU	quarkonium electron trigger
TOF	Time-Of-Flight detector
TPC	Time Projection Chamber
TRD	Transition Radiation Detector
TRU	Trigger Region Unit
TRG	Trigger System
V^0	Unknown Particle
ZDC	Zero Degree Calorimeter

References

[1] K. Aamodt. “Photon, π^0 and η measurements in proton-proton collisions at $\sqrt{s} = 7$ TeV with the ALICE TPC at the LHC”. PHD thesis. University of Oslo, 2011.

[2] K. Aamodt et al. “The ALICE experiment at the CERN LHC”. *JINST* 3 (2008), S08002. DOI: `10.1088/1748-0221/3/08/S08002`.

[3] B. Abelev et al. “Neutral pion and η meson production in proton-proton collisions at $\sqrt{s} = 0.9$ TeV and $\sqrt{s} = 7$ TeV”. *Phys.Lett.* B717 (2012), pp. 162–172. DOI: `10.1016/j.physletb.2012.09.015`. arXiv: `1205.5724 [hep-ex]`.

[4] Betty Bezverkhny Abelev et al. “Neutral pion production at midrapidity in pp and Pb-Pb collisions at $\sqrt{s_{NN}} = 2.76$ TeV” (2014). arXiv: `1405.3794 [nucl-ex]`.

[5] B. Alessandro et al. “ALICE: Physics performance report, volume II”. *Journal of Physics G: Nuclear and Particle Physics* 32 (2006), pp. 1295–2040.

[6] *ALICE webpage*. URL: `http://aliceinfo.cern.ch/Public/Objects/Chapter2/ALICE-SetUp-NewSimple.gif`.

[7] J. Alme et al. “The ALICE TPC, a large 3-dimensional tracking device with fast readout for ultra-high multiplicity events”. *Nucl.Instrum.Meth.* A622 (2010), pp. 316–367. DOI: `10.1016/j.nima.2010.04.042`. arXiv: `1001.1950`.

[8] B. Andersson, S. Mohanty, and F. Söderberg. “Recent developments in the Lund model” (2002). arXiv: `hep-ph/0212122 [hep-ph]`.

[9] DESY Armen Buniatian. “Large Transverse Energies and Jets in Hard Photoproduction at HERA” (1995).

[10] INR RAS Artem Konevskikh. “T0 and V0 cross section from VdM scan, fill 3316” (2013). URL: `https://indico.cern.ch/event/276276/contribution/3/material/slides/0.pdf`.

[11] P. Aurenche et al. “Multiparticle production in a two-component dual parton model”. *Phys. Rev. D* 45 (1 1992), pp. 92–105. DOI: `10.1103/PhysRevD.45.92`. URL: `http://link.aps.org/doi/10.1103/PhysRevD.45.92`.

[12] Vito Manzari – INFN Bari. “Upgrade of the ALICE Inner Tracking System”. 2011. URL: `http://aliceinfo.cern.ch/ITS/sites/aliceinfo.cern.ch.ITS/files/documents/manzari_HSTD8_2011-12-07.pptx`.

[13] J. et al. (Particle Data Group) Beringer. “Review of Particle Physics”. *Phys. Rev. D* 86 (1 2012), p. 010001. DOI: `10.1103/PhysRevD.86.010001`. URL: `http://link.aps.org/doi/10.1103/PhysRevD.86.010001`.

[14] L. Betrev and P. Chochula. “Definition of the ALICE Coordinate System and Basic Rules for Sub-detector Components Numbering”. *ALICE-INT-2003-038 v.2* (2003). URL: `https://edms.cern.ch/document/406391/2`.

[15] J. D. Bjorken. “Energy Loss of Energetic Partons in Quark - Gluon Plasma: Possible Extinction of High p(t) Jets in Hadron - Hadron Collisions” (). FERMILAB-PUB-82-059-THY.

[16] F. Bock. “Neutral Pion and Eta Meson Production in pp and Pb–Pb Collisions at the LHC with the ALICE Detector”. MA thesis. University Heidelberg, 2012. URL: `http://www.physi.uni-heidelberg.de//Publications/Bock-Masterthesis.pdf`.

[17] E Bruna et al. “Vertex reconstruction for proton-proton collisions in ALICE” (2009). URL: `https://cds.cern.ch/record/1225497`.

[18] C.P. Burgess. “Goldstone and Pseudo-Goldstone Bosons in Nuclear, Particle and Condensed-Matter Physics” (1998). eprint: `arXiv:hep-th/9808176v3`.

[19] C.P. Burgess and G.D. Moore. “The standard model: A primer” (2007).

[20] A. Capella et al. “Dual parton model”. *Phys.Rept.* 236 (1994), pp. 225–329. DOI: `10.1016/0370-1573(94)90064-7`.

[21] ALICE Collaboration. “Femtoscopy of pp collisions at $\sqrt{s} = 0.9$ and 7 TeV at the LHC with two-pion Bose-Einstein correlations” (2011). arXiv: `1101.3665 [hep-ex]`.

[22] ALICE Collaboration. “The ALICE Experiment at the CERN LHC”. *Journal of Instrumentation* 08 S08003 (2008).

[23] ATLAS Collaboration. “The ATLAS Experiment at the CERN Large Hadron Collider”. *Journal of Instrumentation* (2008). URL: `stacks.iop.org/1748-0221/3/i=08/a=S08003`.

[24] LHCb Collaboration. “The LHCb Detector at the LHC”. *JINST* 3:S08003 (2008).

[25] P. Cortese et al. “ALICE electromagnetic calorimeter technical design report” (2008).

[26] Lázló P. Csernai. “Introduction to Relativistic Heavy Ion Collisions” (2008).

[27] R. K. Ellis, W. J. Stirling, and B.R. Webber. *QCD and collider physics*. Vol. 8. Cambridge University Press, 1996, pp. 1–435. DOI: `ISBN:978-0521545891`.

[28] R. Engel. “PHOJET manual”. *University of Siegen preprint* (1995), pp. 95–05.

[29] R. Engel, J. Ranft, and S. Roesler. “Hard diffraction in hadron hadron interactions and in photoproduction”. *Phys.Rev.* D52 (1995), pp. 1459–1468. DOI: `10.1103/PhysRevD.52.1459`. arXiv: `hep-ph/9502319 [hep-ph]`.

[30] (ed.) Evans L. and (ed.) Bryant P. “LHC Machine”. *JINST* 3 (2008), S08001. DOI: `10.1088/1748-0221/3/08/S08001`.

[31] Hans Rudolf Schmidt (for the Alice Experiment). “The ALICE TPC: Status and perspectives”. *J. Phys.* Ser. 230 012023 (2010). URL: `http://iopscience.iop.org/1742-6596/230/1/012023`.

[32] R. J. Fries and B. Müller. “Heavy ions at LHC: Theoretical issues”. *Eur.Phys.J.* C34 (2004), S279–S285. DOI: `10.1140/epjcd/s2004-04-026-6`. arXiv: `nucl-th/0307043 [nucl-th]`.

[33] D.J. Gross and F. Wilczek. “Ultraviolet Behavior of Nonabelian Gauge Theories”. *Phys.Rev.Lett.* 30 (1973), pp. 1343–1346. DOI: `10.1103/PhysRevLett.30.1343`.

[34] Francis Halzen and Alan Martin. *Quarks & Leptons: An introductory course in modern particle physics*. New York, USA: John Wiley & Sons, 1984.

[35] Ulrich W. Heinz. *Concepts of Heavy-Ion Physics*. 2004. eprint: arXiv:hep-ph/0407360.

[36] E. M. Henley and A. L. Garcia. “Subatomic Physics”. *World Scientific* (2007).

[37] K. Koch. “Measurement of π^0 and η mesons with photon conversions in ALICE in proton-proton collisions at $\sqrt{s}$ = 0.9, 2.76, 7 TeV”. PhD thesis. University of Heidelberg, 2012. URL: http://www.ub.uni-heidelberg.de/archiv/13113.

[38] *LHC filling schemes*. URL: http://lpc.web.cern.ch/lpc/fillingschemes.htm.

[39] *LHC Luminosity Plots for the 2012 Proton Run*. 2012. URL: http://lpc.web.cern.ch/lpc/lumiplots_2012.htm.

[40] S. Datta J. van der Heide C. Jung F. Karsch O. Kaczmarek E. Laermann R. D. Mawhinney C. Miao P. Petreczky K. Petrov C. Schmidt T. Umeda M. Cheng N. H. Christ. “The transition temperature in QCD”. *Phys.Rev* D74:054507,2006 (2006). DOI: 10.1103/PhysRevD.74.054507. arXiv: hep-lat/0608013 [hep-lat].

[41] A. Marín et al. *ALICE Conversion Software*. URL: http://git.cern.ch/pubweb/AliRoot.git/blob/master:/PWGGA/GammaConv/.

[42] Messel and Crawford. “Electron-Photon Shower Distribution Funcion Tables for Lead, Copper, and Air Absorbers”. *Pergamon Press* (1970).

[43] for the ALICE TRD Collaboration M.J. Kweon. “The Transition Radiation Detector for ALICE at LHC”. *Nucl.Phys.A830:535c-538c* (2009). DOI: 10.1016/j.nuclphysa.2009.10.047. arXiv: nucl-ex/0907.3380 [nucl-ex].

[44] K. Nakamura et al. “Review of particle physics”. *J.Phys.* G37 (2010), p. 075021. DOI: 10.1088/0954-3899/37/7A/075021.

[45] N. Arbor O. Bourrion et al. “The ALICE EMCal L1 trigger first year of operation experience” (2012). arXiv: 1210.8078 [physics.ins-det].

[46] J. Podolanski and R. Armenteros. “ANALYSIS OF V-EVENTS”. *Phil. Mag.* 7 (1954).

[47] H.D. Politzer. “Reliable Perturbative Results for Strong Interactions?” *Phys.Rev.Lett.* 30 (1973), pp. 1346–1349. DOI: 10.1103/PhysRevLett.30.1346.

[48] F. Ronchetti et al. “The ALICE electromagnetic calorimeter high level triggers”. *J.Phys.Conf.Ser.* 396 (2012), p. 012045. DOI: 10.1088/1742-6596/396/1/012045. arXiv: 1209.3647 [physics.ins-det].

[49] *Root webpage*. URL: http://root.cern.ch/.

[50] *Run condition table*. URL: http://alimonitor.cern.ch/configuration/.

[51] N. E. Tyurin S. M. Troshin. “On the double-ridge effect at the LHC”. *Mod. Phys. Lett. A* Vol. 28, No. 9 (2013). DOI: 10.1142/S0217732313500314. arXiv: 1301.2198 [nucl-th].

[52] T. Sjöstrand. “PYTHIA 8 Status Report” (2008), pp. 726–732. arXiv: 0809.0303 [hep-ph].

[53] T. Sjöstrand, S. Mrenna, and P. Z. Skands. “A Brief Introduction to PYTHIA 8.1”. *Comput.Phys.Commun.* 178 (2008), pp. 852–867. DOI: 10.1016/j.cpc.2008.01.036. arXiv: 0710.3820 [hep-ph].

[54] C. Tsallis. "Possible Generalization of Boltzmann-Gibbs Statistics". *J.Statist.Phys.* 52 (1988), pp. 479–487. DOI: 10.1007/BF01016429.

[55] B. G. Zkharov. "Parton energy loss in the mini quark-gluon plasma and jet quenching in proton-proton collisions" (2013). URL: http://arxiv.org/abs/1311.1159v2.

Acknowledgements

First of all, I would like to thank Prof. Dr. Johanna Stachel for giving me the opportunity to carry out my bachelor thesis in her group and to become involved in the ALICE experiment.

Special thanks go to my supervisor PD Dr. Klaus Reygers for his support when I needed help and his guidance during my time in the group.

Furthermore, I would like to thank Prof. Dr. Norbert Herrmann for reading and evaluating my thesis.

I greatly appreciate the intensive guidance and support from Friederike Bock and Lucia Leardini in all physical and technical questions and for proof-reading my thesis. Their criticism and ideas helped me improving my thesis and my understanding of the necessary physical background.

Also I would like to thank for the helpful advices of Dr. Ana Marin, Jochen Klein and Felix Rettig who provided many useful inspirations for my analysis.

During the work on my thesis I had the opportunity to attend the group meetings of the ALICE and the Photon group and to present my results. Their critisism and ideas helped me improving my thesis and therefore I would like to express my gratitude to the group as well.
For the opportunity to visit CERN and the great conversations with the people working for the collaboration I am very grateful. It was a very helpful experience and a great insight in the collaboration.

Finally, I wish to express my gratitude to my parents, my sister and my grandmother for their support of my studies and for proof-reading my thesis.